creative commons

COMMONS DEED

저작자표시-비영리-변경금지 2.0 대한민국

이용자는 아래의 조건을 따르는 경우에 한하여 자유롭게

- 이 저작물을 복제, 배포, 전송, 전시, 공연 및 방송할 수 있습니다.

다음과 같은 조건을 따라야 합니다:

저작자표시. 귀하는 원저작자를 표시하여야 합니다.

비영리. 귀하는 이 저작물을 영리 목적으로 이용할 수 없습니다.

변경금지. 귀하는 이 저작물을 개작, 변형 또는 가공할 수 없습니다.

- 귀하는, 이 저작물의 재이용이나 배포의 경우, 이 저작물에 적용된 이용허락조건을 명확하게 나타내어야 합니다.
- 저작권자로부터 별도의 허가를 받으면 이러한 조건들은 적용되지 않습니다.

저작권법에 따른 이용자의 권리는 위의 내용에 의하여 영향을 받지 않습니다.

이것은 이용허락규약(Legal Code)을 이해하기 쉽게 요약한 것입니다.

Disclaimer

dCollection

공학석사 학위논문

Investigation of Structural Characteristics of Hot Extruded Leaded-Brass Alloy

열간 압출 유연 황동 합금의
구조적 특성에 관한 연구

2023년 8월

서울대학교 대학원
재료공학부
이 지 은

Investigation of Structural Characteristics of Hot Extruded Leaded-Brass Alloy

열간 압출 유연 황동 합금의 구조적 특성에 관한 연구

지도 교수 박 은 수

이 논문을 공학석사 학위논문으로 제출함

2023 년 8 월

서울대학교 대학원

재료공학부

이 지 은

이지은의 공학석사 학위논문을 인준함

2023 년 8 월

위 원 장	한 홍 남	(인)
부위원장	박 은 수	(인)
위 원	이 명 규	(인)

Abstract

Investigation of Structural Characteristics of Hot Extruded Leaded-Brass Alloy

Ji Eun Lee
Department of Materials Science and Engineering
College of Engineering
Seoul National University

The brass alloy (Cu-Zn-based alloy) exhibits excellent ductility, machinability, and oxidation resistance, making it a widely used material for parts related to complex shape processing in oil and gas pipelines, machinery, and ships. However, for leaded-brass alloy (Cu-Zn-Pb alloy) containing lead, the hot extrusion process, while advantageous in producing various products based on die shape and size, introduces challenges due to the temperature rise caused by friction during extrusion. Particularly, in the case of direct hot extrusion, the additional heat generated from friction and plastic deformation results in various process-related defects. Therefore, optimizing the extrusion temperature range is necessary to minimize process-related flaws while conserving energy during extrusion.

This paper focuses on the investigation of the structural characteristics of the leaded-brass alloy during hot extrusion, aiming to comprehend the correlation between microstructure, mechanical properties, and machinability. Specifically, for

the industrially relevant $Cu_{58}Zn_{39}Pb_3$ wt.% alloy, known for its superior machinability, we meticulously observed the microstructure changes during hot extrusion at different temperatures and specimen locations. The analysis revealed variations in microstructural homogeneity based on the temperature regions where extrusion occurred, considering the presence of the Widmanstätten structure in the cast specimen. Additionally, we interpreted the mechanical properties, assessed through Vickers hardness test and uniaxial tensile test, in relation to the microstructural homogeneity. Finally, drilling tests were conducted to explore the relationship between microstructure, mechanical properties, and machinability. The results confirmed that extrusion at temperatures lower than the β phase's equilibrium temperature in the phase diagram was achievable with stable extrusion within the single β phase region, even when subjected to heat during plastic deformation. Furthermore, we identified that achieving an isotropic blocky α phase with a uniform distribution of Pb particles played a crucial role in enhancing machinability. Based on these findings, this paper is expected to contribute to the optimization of the hot extrusion process for flexible brass alloys at an industrial scale, effectively minimizing process-related flaws while conserving energy through temperature control.

Keywords: Leaded-brass, Hot extrusion, Extrusion temperature, Mechanical property, Machinability

***Student Number*:** 2021-24715

Tables of contents

List of Tables

List of Figures

CHAPTER 1.

Introduction

1.1 Brass alloy

1.1.1 Definition and Characteristics

The brass alloy is a golden ductile alloy composed of Cu and Zn, and has the advantage of excellent corrosion resistance, formability, and machinability, as well as low cost.[1, 2] Due to these characteristics, it is widely used in the industry as a material for machinery and ships, as well as parts related to oil and gas pipelines such as faucets and gas valves that require complex shape processing. [3] In the brass alloy, the Zn content is present in a wide range, and accordingly, different phases are formed, thereby changing mechanical properties and machinability. Depending on the composition, brass alloys are classified into three types: alpha-brass, alpha+beta brass, and beta brass. [1, 4, 5]

Brass alloys can be divided into Low Zn Brass with 5 ~ 20 wt.% of Zn content and High Zn Brass with 20 ~ 45 wt.% and show different physical and mechanical properties depending on the Zn content. [6]

More specifically, as shown in Figure 1.1, when Zn is less than 35 wt.%, it is called α-brass. The lattice structure of the α phase is face-centered cubic (fcc), and this configuration in the lattice structure leads to low strength and high ductility. [4] Therefeore, with these properties, the α-brass is commonly designated as cold

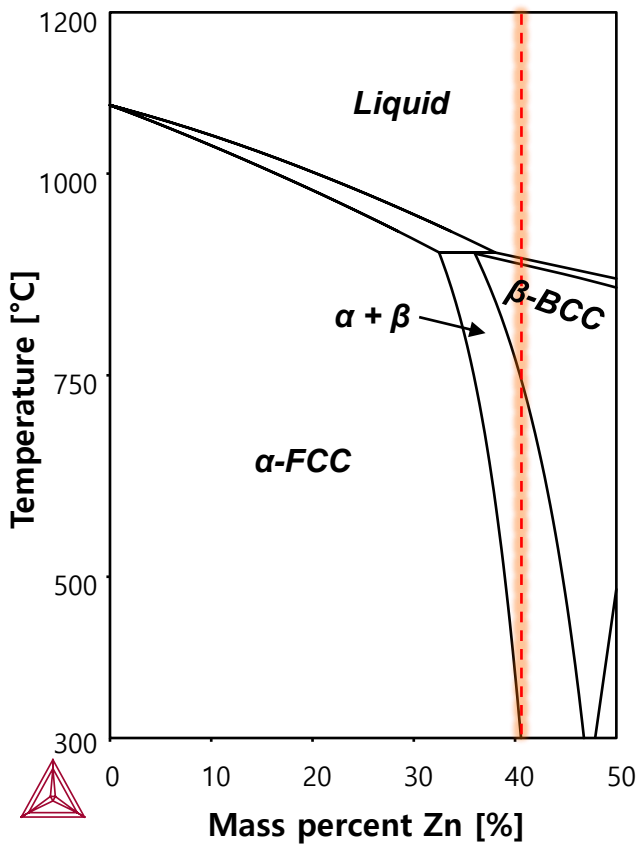

Figure 1.1 Equilibrium phase diagram of binary Cu-Zn system calculated by Thermo-Calc software using SSOL6 database.

working brass. [4]

In the range of the Zn content of 35 ~ 42 wt.%, the brass alloy exists as a dual phase composed of face-centered cubic (fcc) α phase and body-centered cubic (bcc) β phase(which orders at temperatures below ~ 450 ℃ to form β'), which is commonly denoted as duplex brass or α + β brass. [4, 7] Since the lattice structure of the β-phase which is BCC is much harder than the α-phase which is ductile FCC, duplex brass has higher tensile strength and hardness than α-brass. [4] The β-phase has lower resistance to dezincification corrosion than the α-phase, therefore duplex brasses are often geat treated in elevated temperatures in order to decrease the β-phase fraction in the microstructure. Thus, duplex brass is occasionally denoted as hot working brass. [4] The α-FCC phase has good cold workability and excellent corrosion resistance, while the β-BCC phase has excellent plasticity at elevated temperatures, so that complex geometries can be formed through deformation processing. [7] Therefore, these duplex brasses, consisting of α + β phases, are widely used in the plumbing industry to manufacture valves and faucets for transporting potable water. [7] This is due to its good mechanical properties, excellent corrosion resistance, and suitability for thermomechanical processing such as extrusion, forging and machining. [7]

When the Zn content exceeds 45 wt.%, a new phase, γ-phase, appears in the grain boundaries on the microstructure and it makes the brass too brittle. [4]

A cutting process is included in the process of producing brass alloys being processed into their final form, and therefore machinability is a very important characteristic for brass. [4]

Therefore, in this study, in order to study brass alloys with excellent machinability

for use as faucets, the duplex brass area consisting of α + β phases was investigated closely, considering the characteristics of each phase in brass alloys.

1.2 Leaded-brass alloy

1.2.1 Definition and Characteristics

Small amounts of additive elements can be added to brass alloys to improve various mechanical properties. Among them, leaded-brasses containing roughly 1 ~ 3 wt.% of lead have been most widely used to improve machinability. This alloy has the advantage of significantly enhancing the machinability through lowering cutting force, reducing tool wear, improving chip breaking, increasing lubricity, and having better surface quality. [4, 8-10] In leaded-brass composed of α, β, and Pb phases, the distribution and area fraction of the β phase and lead particles contribute to limiting the grain growth and grain coarsening of the α phase. [11]

1.2.2 Role of Pb on machinability

There are two main reasons why leaded-brass has excellent machinability properties, first because lead exists as a insoluble precipitate, and secondly, lead has low melting point. Since lead has a positive heat of mixing with copper, it is insoluble in the brass alloy and dispersed into discrete fine globule particles typically less than 5 μm, causing good chip fragmentation. [11, 12] In brass, the lead inclusion has a spherical shape throughout the grain boundaries and grains. [13] Lead-favored enrichment sites are mainly at the α/β interphase boundary. [14, 15] In addition, lead has a low melting point and is mainly in a molten state during casting and hot working processes, and tends to reduce surface energy by taking a spherical shape. [14, 15] The reason why low cutting force is required when cutting leaded-brass is mainly due to the deformation of lead inclusions segregated in the primary deformation zone. [8] As shown in Fig 1.2, the highly deformed lead particles stretch along the shear plane and change shape from globular to flake-like inclusions, acting as crack initiators in the brass matrix, enforcing a discontinuous chip formation process. [8] In addition, lead has a lower melting point (327.5 ℃) than brass matrix, and during cutting, the thin, semi-liquid lead film significanty reduces friction in the cutting zone and it reduces cutting forces and tool wear. [4, 16-18] Lead segregates throughout the entire microstructure, mainly at the grain boundaries due to their high interfacial energy. [11, 17] This significantly reduces the shear strength, resulting in improved chip breakage where small discontinuous chips are formed. [4, 17] And that discontinuity promotes fast chip breaking, therefore, the cutting force and tool wear are significantly reduced. [11]

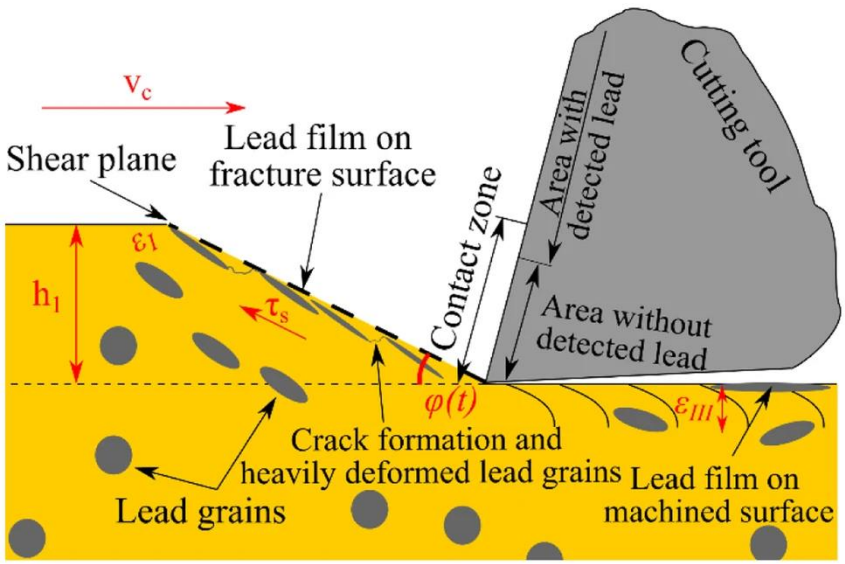

Figure 1.2 Graphical summary of observed mechanism related to enhanced machinability of leaded brass alloys. [8]

A closer look at the mechanism by which lead improves machinability during leaded-brass cutting is as follows. The temperature of the primary shear zone is much lower than the melting point of lead, and discontinuous chip segments are formed as ductile fracture occurs along the shear instability leading from the tool's cutting edge to the free surface. [19] Shear fracture is initiated by the formation of voids at the lead particles that arise from the combined stress of machining and differential thermal expansion. [19] The major function of lead in the secondary shear zone is to provide low-strength regions, where inclusions are stretched out in the chip and provide internal lubrication when the chip passes through the rake face. [19] Lead is drawn out of the cup lets formed during the secondary shear and deposited on the tool surface, eliminating the tendency to built-up-edge formation. [19] The temperature at the end of the contact zone exceeds the melting point of the lead and lead globules deposit on the tool at the rear of the contact length. [19] This is also related to a slight decrease in the rake-face force and secondary shear zone strength, but the internal lubrication of lead has a dominant influence. [19]

1.2.3 Assessment factors and measurement of machinability

Machinability is a complex concept that varies according to multiple parameters and factors, lacking a precise and unambiguous definition. [4, 20] It is generally described as the ability of a material to be machined, but its definition is not straightforward due to its strong dependence on the product itself. [4] The interpretation of machinability can vary among different machining operators, adding to its complexity. [20] $Jönsson\ et\ al.$[20] categorized the intricate notion of machinability into five main evaluation criteria: cutting force and power consumption, chip formation, cutting tool wear, surface properties of the machined workpiece, and environmental factors. [20]

Cutting force is directly related to the power consumption of the process, making the evaluation of cutting forces an essential factor in characterizing the productivity of the process. [4] Tool wear is directly linked to the tool's lifespan, allowing for the consideration of process efficiency. [4] In the industry, tool wear during brass alloy machining is sometimes regarded as a minor issue and, therefore, not always considered as an evaluation factor. [4]

In machining operations such as drilling, milling, and tapping, chip evacuation plays a crucial role, making the assessment of machinability in terms of chip formation highly significant. [4] The presence of undesirable chip formations can substantially hinder chip evacuation efficiency. [4] The occurrence of long and continuous chips poses a higher risk of entanglement within the machinery, leading to obstructions in the cutting zone and potentially causing damage to the cutting tool, workpiece, and the machine itself. [4]

The Pb content and dispersion of Pb particles have played a crucial role in the machinability of the material, and a finer and more homogeneous distribution of Pb particles has resulted in a stronger chip-breaking effect during cutting processes, primarily offers the following advantages: Enhanced machining efficiency for increased productivity, Reduced cutting forces, Improved surface quality of the workpiece, and Diminished tool wear leading to prolonged tool lifespan. [21]

1.3 Hot extrusion process

1.3.1 Thermomechanical process

Brass materials go through various processing processes up to the production of prototypes. Thermomechanical processing is certainly one of the most important methods for conditioning final mechanical features of the plastically deformed products. [22] Leaded-brass rods are produced by hot extrusion and drawing and are used as raw materials in the production of a wide range of products from decoration and architecture to electrical/electronic and structural systems. [3] In order to manufacture metal products into desired shapes, mechanical working or forming by plastic deformation is performed. [23] In the plastic working process, in order to obtain the desired shape and size for metal products, ingots or billets are reduced to make semi-finished products with simple shape. [23, 24] In general, it is divided into hot working and cold working according to the processing temperature. And plastic deformation of a material above the recrystallization temperature can be classified as hot working , and below the recrystallization temperature as cold working. [23] The process temperature is an important factor because desired results can be obtained by properly and specifically setting the temperature of hot working processes such as rolling or extrusion.

1.3.2 Direct Extrusion

Since the extrusion process has more severe plastic deformation than rolling, it is possible to make through extrusion what was not able to produce by rolling, and because of the lower deformation resistance of metal at a elevated temperature, hot extrusion is performed to reduce the large force required for extrusion. The process of putting a billet into a container(chamber) and pushing it out through a die orifice of the desired shape by applying high pressure to the ram is called extrusion. [23, 25] This process is widely used in copper and aluminium alloys to reduce the cross-sectional size of metal casting billets to produce bar, wire and tube. [23, 25]

It is divided into direct extrusion and indirect extrusion according to the moving direction of the ram(stem) and metal flow in the extrusion machine. [26] In the case of direct extrusion, since the billet moves, the frictional resistance between the billet and the container wall is high. [23] Frictional stress existing at the interface between the container and the billet generates heat, so the surface temperature of the billet rises, resulting in a high tendency to form surface defects. Also, due to high friction and temperature, the service life of the extrusion toolng is relatively short. [23]

1.3.3 Factors influencing extrusion

Since the final product is produced through cutting after extrusion, machinability is important in brass, and this machinability is greatly affected by hot extrusion conditions. [25]

During extrusion process, the ratio of the crossectional area of the initial billet and the extrudate is known as the extrusion ratio and it is mathmetically defined by:

$$\boldsymbol{Extrusion\ ratio, R} = \frac{A_1}{A_2} \tag{1.1}$$

A_1 is the initial cross-sectional area of the billet before extrusion and A_2 is the final cross-sectional area of the finished product after extrusion. In this research, calculated value is 20.25 with as-cast billet of 180mm diameter and final extruded rod product of 20mm diameter. This can be compared not by area but by diameter, and the extrusion ratio according to the diameter ratio calculated with the specimen in this study is 9.

The microstructure, texture, and mechanical properties of the extrudates are notably influenced by two key process parameters: the temperature of the billet and the extrusion ratio. [24] The material's flow stress or deformation resistance decreases as the temperature increases. To capitalize on this effect, hot extrusion is commonly employed for most metals. However, once the heated billet enters the preheated chamber and the extrusion process begins, the billet's temperature during extrusion becomes influenced by factors that generate heat within the billet and those that transfer heat from it. Given these challenges, it is beneficial to use the minimum working temperature that provides suitable plasticity to the metal. If the surface temperature of the extrudate reaches the critical temperature where hot shortness

occurs, surface defects may arise. The temperature of the extruded part upon exiting the die is a critical process variable that significantly impacts the quality of the extrudate. Therefore, it is desirable to control the exit temperature of extrusion and maintain a constant extrusion temperature at the exit point. [23]

1.3.4 Metal flow and extrusion defects

During billet extrusion, the metal flow pattern differs depending on the symmetry of the die arrangement. [23] If the billet is longitudinaly bisected and the two halves are joined together and extruded through an axially positioned die, the actual flow of the cut billet will be the same as that of the uncut billet, but if the die is asymmetrically arranged, the flow will clearly be affected by the cutting. [23] After extrusion, the flow patterns were quantitatively evaluated based on the degree of distortion of the grid. [23] The results revealed that the flow behavior of the billet within the extrusion chamber undergoes distinctive changes depending on the process employed and the material being extruded. [23] The primary cause of these variations is attributed to the difference in frictional resistance between the billet and the extrusion chamber wall. [23] It is classified into four types of ‘S’, ‘A’, ‘B’, and ‘C’ according to the order of increasing non-uniformity of the flow. [23]

Flow pattern ‘B’ occurs in homogeneous materials when significant interface friction exists at both the container wall and the surface of the die and its holder. [23] Friction at the billet/container interface slows down material flow in peripheral zones while the central region experiences less resistance, resulting in a velocity gradient across the billet’s cross-section. [23] This creates a large dead-metal zone that forms

at the die shoulders. [23] During extrusion initiation, shear deformation is concentrated in peripheral regions, but it spreads toward the center as deformation progresses. [23] This raises the risk of materials, along with lubricants, oxides, or impurities, flowing from the billet surface along the shear zone and extruding as defects into the interior of the extruded product. [23] Flow pattern 'B' is commonly observed in single-phase homogeneous copper alloys that lack a lubricating oxide film on the surface and in most aluminium alloys (Laue and Stenger 1981). [23]

Flow pattern 'C' is commonly observed during the hot extrusion of inhomogeneous materials. [23] This flow pattern occurs when there is significant interface friction, which hinders the flow of surface material similar to flow pattern 'B'. Additionally, it can be present when the billet surface is exposed to chilling effects from the walls of a cold chamber, resulting in a considerably higher flow stress in the cold surface material compared to the hot material in the core. [23] As a consequence of these conditions, the stronger material in the funnel becomes plastic and undergoes severe plastic deformation, particularly in the shear zone, as it moves towards the die during extrusion. [23] During the extrusion process, the stiff shell and dead-metal zone experience axial compression, leading to the displaced material from the outer zones following the path of least resistance to the back of the billet. [23] Subsequently, this material turns towards the center and flows into the funnel (Laue and Stenger 1981). [23] This flow pattern gives rise to an internal extrusion defect, which manifests as an annular ring of oxide in the cross-section at the rear end of the extruded product. [23] The defect is caused by the flow of oxidized surface material into the extrusion. [23] Flow pattern 'C' is typically observed in the hot extrusion of $\alpha + \beta$ brasses, and this is attributed to the cooling of the billet surface,

resulting in an increase in the flow stress in the surface regions. [23] Flow pattern ‘C’ will occur when a hard billet shell exists, and simultaneously, there is high friction at the container wall. [23]

In this study, type ‘C’ and type ‘B’ are mentioned in Section 4.2.1.

There is a disadvantage that the process waste is 10~15% in extrusion, while rolling is 1 to 3%. [23] In the hot extrusion process, the forward end of the extrudate experiences minimal deformation, particularly when extruding cast ingots. [23] Consequently, the cast structure of the material can persist in the central zone of the extrudate, even at a high extrusion ratio (ratio of cross-sectional areas of unextruded to extruded billet) of 15. [23] Thus, it becomes essential to remove or crop the leading end of the extrudate to eliminate any potential defects resulting from the retention of the original cast structure. [23]

1.4 Thesis objective and strategy

In this study, a comparison of the microstructure of as-cast and hot-extrusion was conducted to understand the change in microstructure during extrusion. In addition, hot extrusion is carried out at a temperature slightly lower than the actual process temperature, and a temperature range in which uniform materials are formed is proposed through microstructure and mechanical property analysis. In addition, 'C' pattern and 'B' pattern were observed among the metal flow types of the leaded-brass extrusion process, and this study intends to understand them separately. Until now, previous studies have compared the temperature of the α + β region with the β region, but we have conducted experiments on different α + β regions, considering that there is a temperature increase during direct extrusion.

CHAPTER 2

Experimental procedures

2.1. Sample preparation

2.1.1 Fabrication of leaded brass alloy rod

Ingots of duplex leaded-brass alloy with a composition of 58 wt.% Cu, 39 wt.% Zn, and 3 wt.% Pb, along with duplex lead-free brass alloy containing 60 wt.% Cu and 40 wt.% Zn, were produced using a high-frequency induction melting system (Pillar Industries, USA) operating at 400 V and 500 kW. The fabrication process involved the use of high-purity raw materials, including Cu(99.98%), Zn(99.98%), and Pb(99.98%), to ensure compositional homogeneity. A schematic time-temperature processing diagram of the casting and thermomechanical treatment processes is presented in Figure 2.1.(a). To achieve compositional homogeneity, each as-cast ingot underwent a heating process in the high-frequency induction furnace at 1070 ℃ for 70 minutes. The as-cast Cu58Zn39Pb3 wt.% and Cu60Zn40 wt.% alloys were then shaped into cylinders with a diameter of 180 mm and a height of 400 mm, followed by air-cooling.

The subsequent hot extrusion processes were conducted at two different temperatures: 670 ℃ (0.82 Tm) and 730 ℃ (0.87 Tm). Prior to the hot-extrusion process, the ingots were heated up to 700 ℃ and inserted into a container of a direct extrusion press (SMS group Inc., USA). The extrusion was carried out using a die with a diameter of 20 mm, and the forward movement of the ram at 440 V and 1500

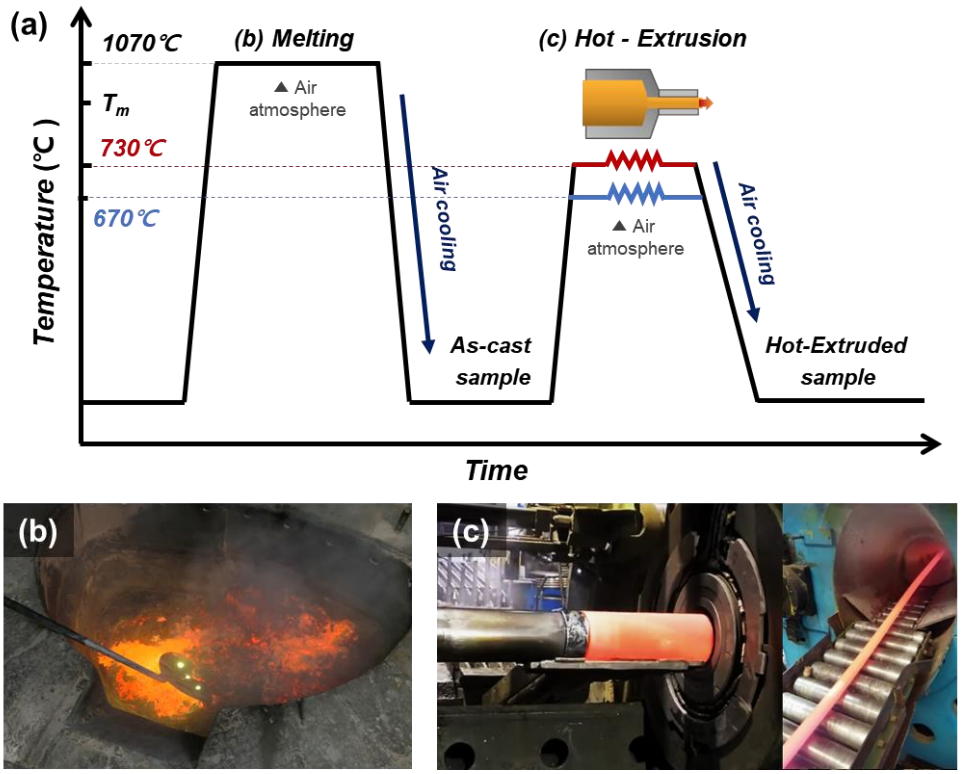

Figure 2.1. (a) A schematic time-temperature processing diagram of casting and thermomechanical treatment processes. Photos of (b) casting process with the sample dimension of 180 mm (diameter) x 400 mm (height), and (c) hot-extrusion process with the sample dimension of 20 mm (diameter) x 27 m (height).

kW for 10 seconds. The extrusion process resulted in cylindrical rod-shaped specimens with a diameter of 20 mm and a length of 27 m, as depicted in Figure 2.1.(c).

2.2 Phase diagram calculation

The pseudo-binary equilibrium phase diagram of Cu60Zn40 – Pb in Cu-Zn-Pb ternary alloy system was calculated by Thermo-Calc software using SSOL6 database. The calculated phase diagram was useful in understanding the phase transition and monotectic reaction of brass and Pb. The equilibrium phase fraction of the alloy and the composition of each phase according to the temperature were also confirmed with a phase diagram and table.

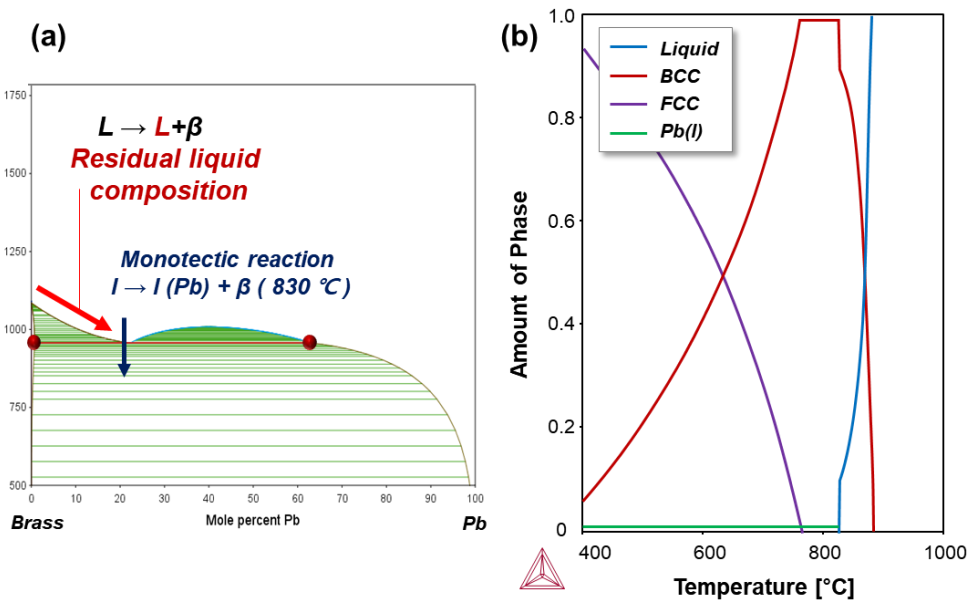

Figure 2.2. (a) Pseudo binary phase diagram of ($Cu_{60}Zn_{40}$) - Pb alloy system and (b) Equilibrium phase diagram of $Cu_{58}Zn_{39}Pb_3$ wt.% alloy with one axis diagram for amount of phase calculated by Thermo-Calc software using SSOL6 database.

Temp [℃]	Liquid#1				BCC - β				FCC - α				Liquid#2 (Pb-rich)			
	Cu	Pb	Zn	Phase fraction	Cu	Pb	Zn	Phase fraction	Cu	Pb	Zn	Phase fraction	Cu	Pb	Zn	Phase fraction
890	58.000	3.000	39.000	1.000												
885.8	58.000	3.000	39.000	1.000	61.091	0.243	38.666	0								
880	56.657	4.198	39.145	0.691	60.400	0.371	39.230	0.309								
870	54.601	6.724	38.675	0.403	60.019	0.499	39.483	0.597								
860	52.670	9.604	37.726	0.262	59.778	0.618	39.605	0.738								
850	50.739	12.731	36.531	0.183	59.610	0.723	39.667	0.817								
840	48.734	16.103	35.163	0.134	59.486	0.814	39.699	0.866								
830	46.582	19.791	33.627	0.102	59.483	0.817	39.700	0.898					1.628	96.878	1.494	
829.4	46.370	19.890	33.740	0.000	59.311	0.817	39.872	0.992					1.615	96.877	1.508	0.008
820					59.311	0.817	39.872	0.992					1.501	97.108	1.391	0.008
810					59.338	0.771	39.891	0.992					1.391	97.330	1.279	0.008
800					59.392	0.679	39.929	0.992					1.292	97.531	1.177	0.008
790					59.418	0.636	39.946	0.992					1.202	97.714	1.084	0.008
780					59.442	0.594	39.963	0.992					1.120	97.880	1.000	0.008
770					59.465	0.555	39.980	0.992					1.045	98.033	0.922	0.008
766.06					59.474	0.540	39.986	0.992	63.806	0.705	35.490	0.000	1.017	98.090	0.894	0.008
760					59.349	0.518	40.133	0.961	63.723	0.676	35.600	0.031	0.969	98.171	0.860	0.008
750					59.147	0.483	40.370	0.913	63.590	0.632	35.778	0.079	0.896	98.296	0.808	0.008
740					58.950	0.450	40.600	0.867	63.461	0.589	35.950	0.125	0.829	98.413	0.758	0.008
730					58.757	0.419	40.824	0.823	63.334	0.549	36.117	0.168	0.767	98.521	0.712	0.009
720					58.570	0.389	41.041	0.782	63.211	0.510	36.279	0.209	0.709	98.623	0.668	0.009
710					58.386	0.361	41.253	0.743	63.090	0.474	36.436	0.248	0.656	98.717	0.627	0.009
700					58.207	0.334	41.460	0.706	62.972	0.439	36.589	0.286	0.607	98.805	0.588	0.009
690					58.031	0.308	41.660	0.670	62.856	0.407	36.737	0.321	0.561	98.888	0.551	0.009
680					57.860	0.284	41.856	0.636	62.743	0.376	36.882	0.355	0.519	98.965	0.517	0.009
670					57.691	0.262	42.047	0.604	62.631	0.346	37.022	0.387	0.479	99.037	0.484	0.009
660					57.527	0.241	42.232	0.573	62.522	0.319	37.159	0.418	0.443	99.105	0.453	0.009
650					57.366	0.221	42.414	0.543	62.415	0.293	37.292	0.448	0.408	99.168	0.423	0.009

Table 2.1. Equilibrium phase fraction and composition of each phase depending on the temperature of $Cu_{58}Zn_{39}Pb_3$ wt.% alloy calculated by Thermo-Calc software using SSOL6 database.

2.3 Thermal analysis

2.3.1 Differential Scanning Calorimetry (DSC)

The differential scanning calorimetry (DSC, DSC 404 F3 Pegasus, Netzsch, Germany) was employed to investigate the phase transformation behavior depending on the temperature. It was first measured with an empty crucible and used as a blank reference. The 12.3mg $Cu_{58}Zn_{39}Pb_3$ as-cast sample was put in a Al_2O_3 crucible for the measurement. The measurement was performed with a heating rate of 10 K min^{-1} for the temperature range from 150 ℃ to 1000 ℃ in Ar gas atmosphere.

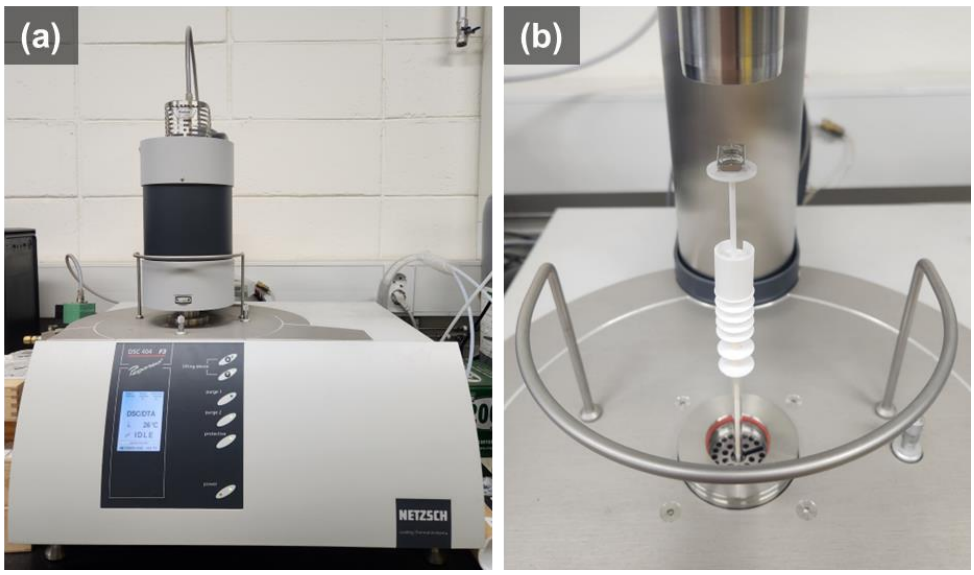

Figure 2.3 (a) The overview of the differential scanning calorimetry (DSC; DSC 404 F3 Pegasus, Netzsch, Germany) (b) The detailed image of the sample carrier

2.4 Structural analysis

2.4.1 X-ray diffraction (XRD)

The crystal structures and the constituent phase for each sample were identified by an X-ray diffractometer (XRD; D2 phaser, Bruker, USA) with Cu Kα radiation at room temperature. The experiments were conducted under a condifion of θ–2θ mode from 20 to 80 degrees and the exposure time was 1.5 seconds per degree.

2.4.2 Optical Microscope (OM)

To observe the microstructural characterization clearly, the specimens were prepared from hot mounting, grinding, polishing, and chemical etching in order. Specifically, grinding was performed using sanding sheet from 100 grit to 2000 grit with water, followed by fine polishing with 6 μm and 1 μm with diamond suspensions. Chemical etching was conducted with etching solution of nitric acid and distilled water (1:1, 50 vol%) for about 3 seconds. Microstructure imaging analysis was performed with an optical microscope (Nikon Eclipse LV150, Nikon, Japan) and image analysis sofrware (ImageJ, Laboratory for Optical and Computational Instrumentation; LOCI, USA).

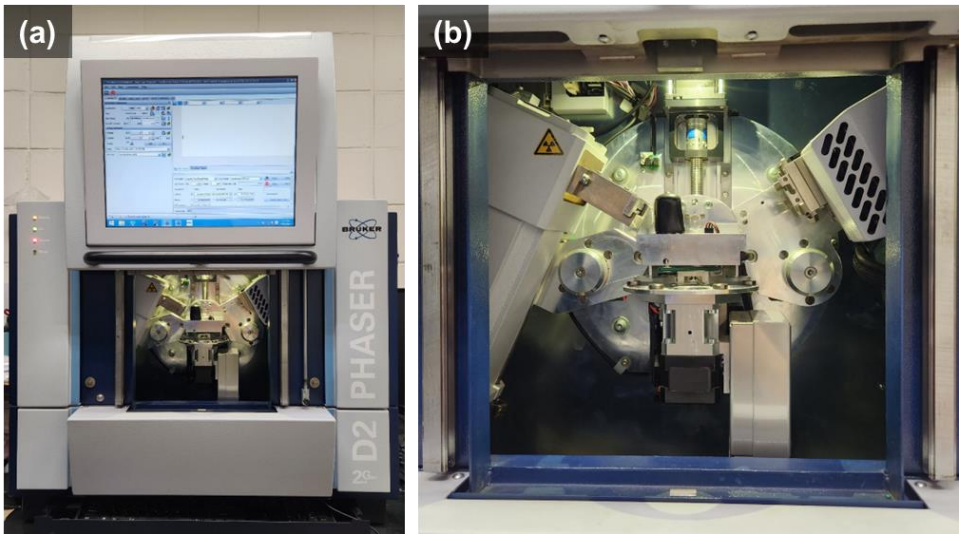

Figure 2.4 (a) The overview of the X-ray diffractometer (XRD; D2 phaser, Bruker, USA) (b) The detailed image of the sample stages and detector

Figure 2.5 The overview of the optical microscope (OM; Nikon Eclipse LV150, Nikon, Japan)

2.4.3 Scanning electron microscopy (SEM)

A field-emission scanning electron microscope (FE-SEM; MIRA3, Tescan, USA) observations were conducted using secondary electron (SE) imaging and backscattered electron (BSE) detectors. The composition analysis was carried out with energy-disperse X-ray spectroscopy (EDS; xFlash 6130, Bruker, USA).

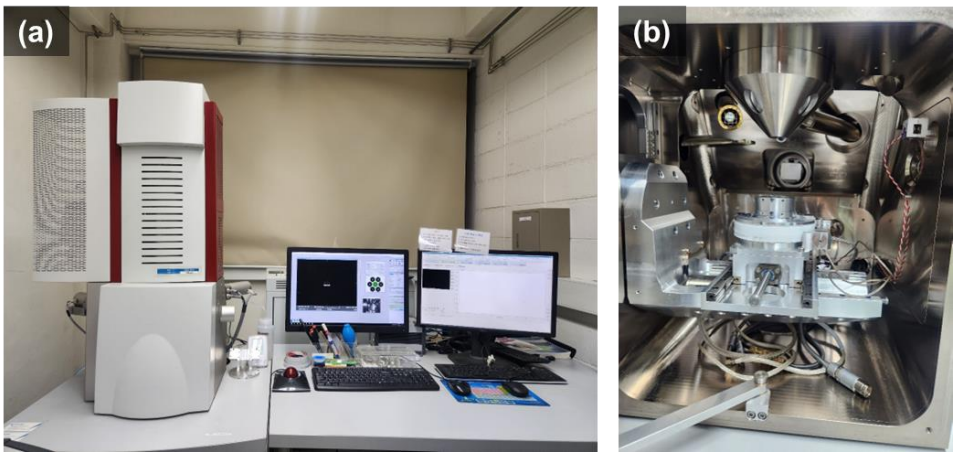

Figure 2.6. (a) The overview of the a field-emission scanning electron microscope (FE-SEM; MIRA3, Tescan, USA) and energy-disperse X-ray spectroscopy (EDS; xFlash 6130, Bruker, USA) (b) The detailed image of the sample stages and detector of SEM

2.5 Mechanical analysis

2.5.1 Uniaxial tensile test

Uniaxial tensile tests were carried out using the universal mechanical tester (Instron 5967, Instron, USA). For experiment, specimens were prepared in shape of dog-bone type with a gauge length of 12mm. Uniaxial tensile tests were conducted with a strain rate of $1 \times 10^{-3}\ s^{-1}$ at room temperature.

2.5.2 Vickers hardness test

Vickers hardness tests were carried out using a microhardness tester (DuraScan 70, Emco-test, Austria) under a load of 1kgf at room temperature. To minimize experimental errors and obtain an average value, sixty points measurements were performed for each sample.

Figure 2.7 The overview of the universal mechanical tester (Instron 5967, Instron, USA)

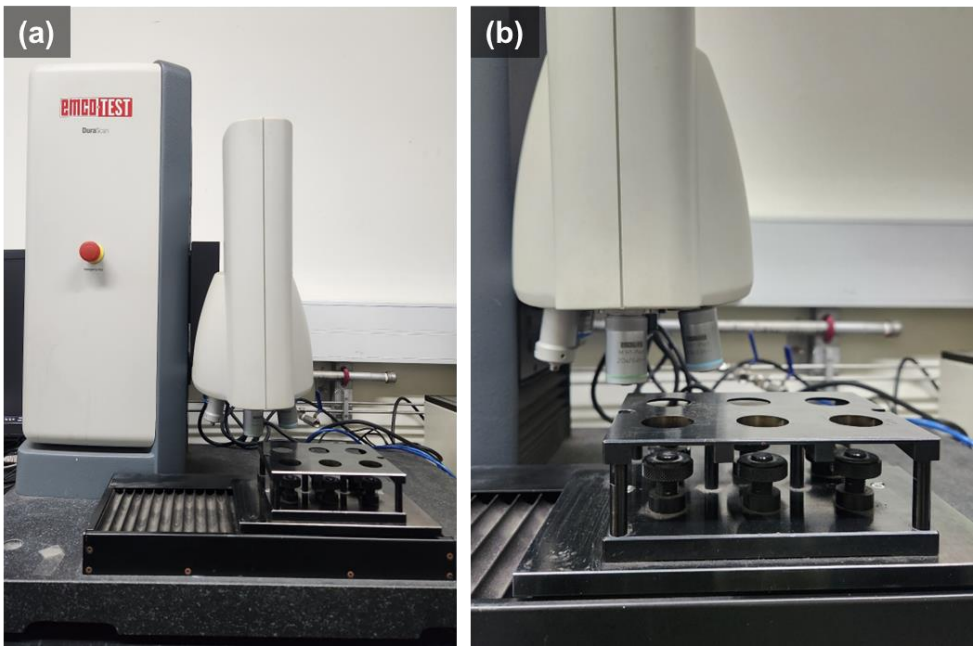

Figure 2.8 (a) The overview of the microhardness tester (DuraScan 70, Emco-test, Austria) (b) The detailed image of the sample stages and indentor

2.6 Machinability drilling test

Machinability evaluation was carried out using a drilling tester (HITAP Servo Tapping Machine HT300, HANSHIN ROBO TECH , Korea). The drilling tests were conducted with a 7mm diameter PVD TiN and TiAlN coated carbide drill (YSD 070, YesTool, Republic of Korea). Specifically, experimental conditions were set as follows: spindle rpm was 1500rpm, spindle stroke was 27mm, and drilling speed was 3mm/sec.

$Cu_{60}Zn_{40}$ wt.% lead-free brasses with a diameter of 15mm and a height of 30mm, hot extruded $Cu_{58}Zn_{39}Pb_3$ wt.% leaded-brasses at each temperature 670°C and 730°C with a diameter of 20mm and a height of 50mm. Experiments were carried out more than three times per specimen. Then, the average value was obtained and evaluated for comparison with respect to the samples under each condition.

During the drilling test, the rotational torque was measured at each data point, and machinability was evaluated by determining how much the amount of load applied during material processing was reduced in comparison with the maximum rotational torque value 4.77Nm. In addition, chips generated during drilling tests were collected and the morphology, size, and weight of the chips were analyzed.

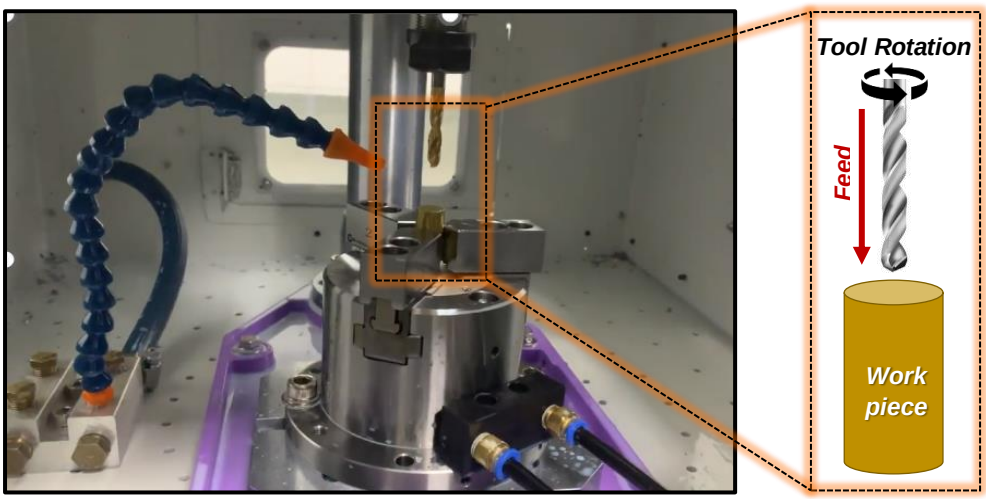

Figure 2.9. The overview of an in-house designed drilling machine (HITAP Servo Tapping Machine HT300, HANSHIN ROBO TECH, Republic of Korea) and the detailed schematic description of drilling operation for evaluation of machinability

CHAPTER 3

Comparison of as-cast and hot-extruded microstructure

3.1. Solidification and phase transformation of as-cast alloy

Figure 3.1 shows the OM microstructure images of $Cu_{58}Zn_{39}Pb_3$ leaded-brass alloy. As described in 1.1 to 1.2 above, the leaded-brass alloy is composed of α-FCC, β-BCC, and Pb phases, which was also confirmed through the XRD peaks in Figure 3.2 The OM image shows that the α-FCC phase has a $Widmanstätten$ structure due to the crystallographic orientation relationship between FCC and BCC. Distribution of each phase can be confirmed through EDS mapping images as shown in Figure 3.3 Since Pb does not have solubility in Cu and Zn, it forms immiscible particles and appears in size of 1.8 $\pm$ 0.5 μm.

According to previous studies, it is known that lead prefers to be dispersed at interphase boundaries with high interfacial energy. [11, 14, 15, 21] However, in the case of as-cast specimens, lead particles were distributed not only at the α/β boundary but also inside the α-FCC phase. There are previous papers that reported this phenomenon[5, 27], the eutectic reaction during solidification of leaded-brass forms spherical inclusions of nearly pure Pb along the grain boundaries and throughout the matrix. This paper aims to understand the non-uniform distribution of lead particles in as-cast specimens based on the solidification phenomenon.

Figure 3.4 schematically shows the microstructural evolution during the

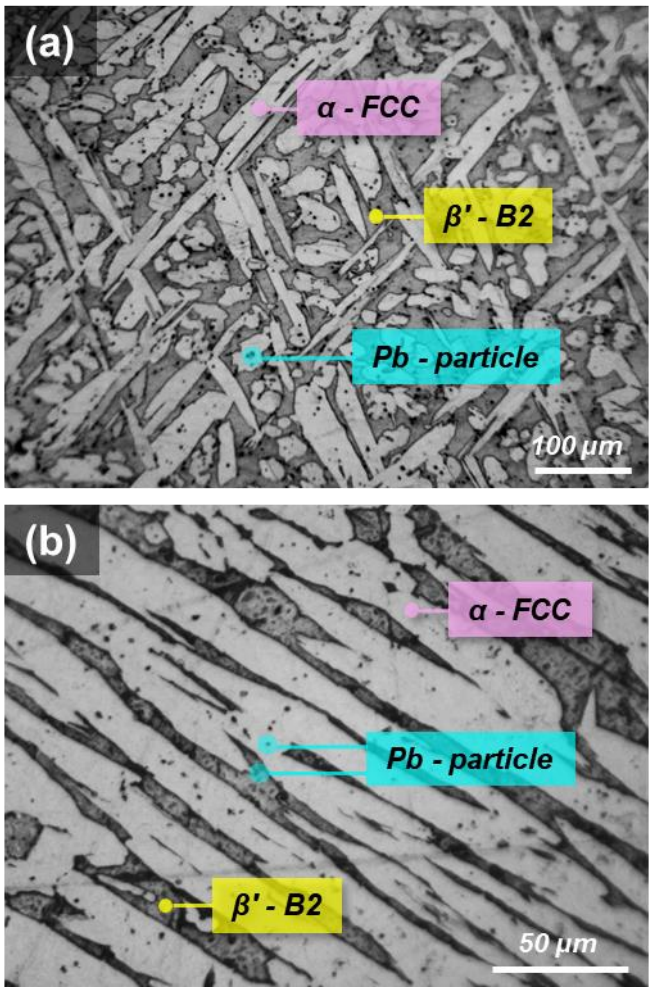

Figure 3.1. (a), (b) Optical microscope images of as-cast of $Cu_{58}Zn_{39}Pb_3$ wt.% alloy

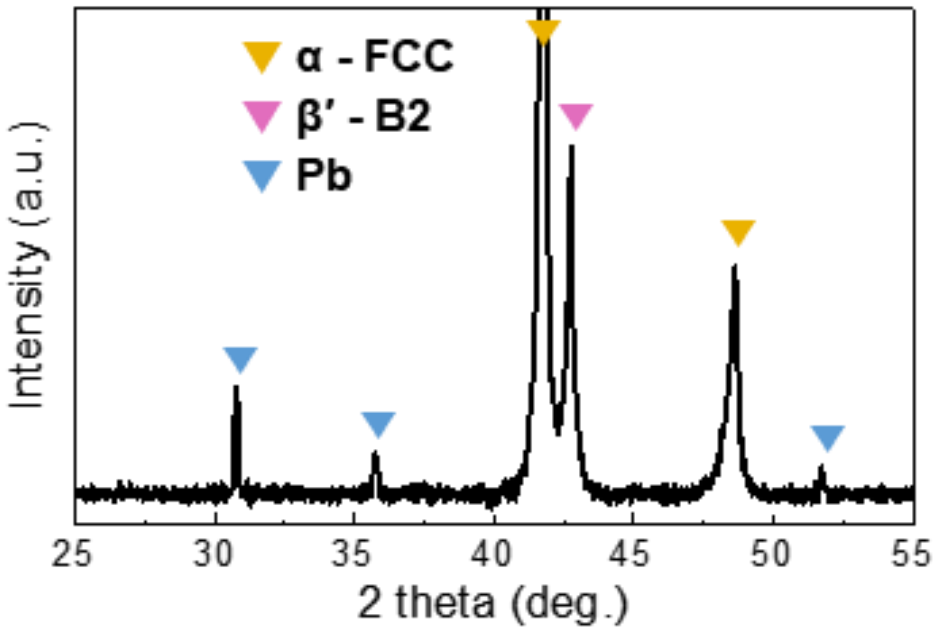

Figure 3.2. XRD pattern of as-cast of $Cu_{58}Zn_{39}Pb_3$ wt.% alloy

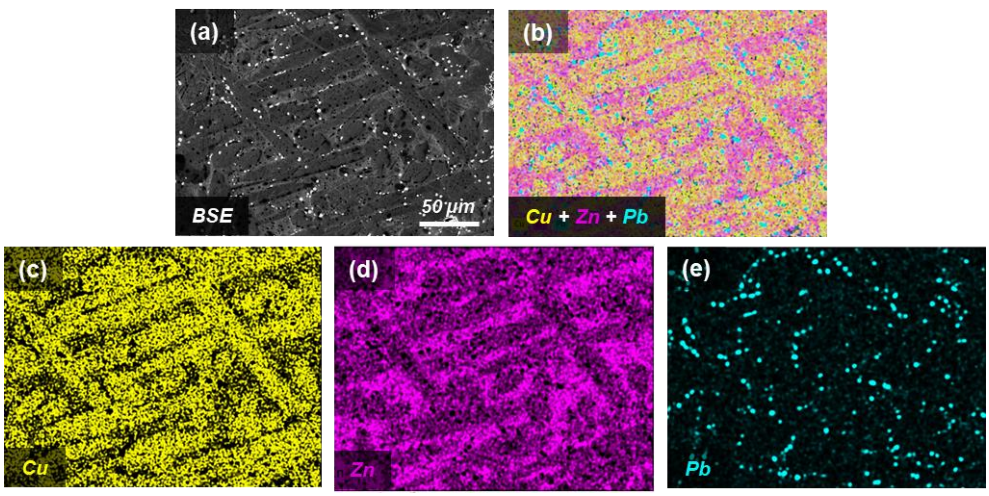

Figure 3.3. (a) SEM images of as-cast $Cu_{58}Zn_{39}Pb_3$ wt.% alloy obtained using backscattered electron detector and (b)-(e) energy dispersive spectroscopy maps showing the distribution of elements Cu (yellow), Zn (pink), and Pb (sky blue), respectively

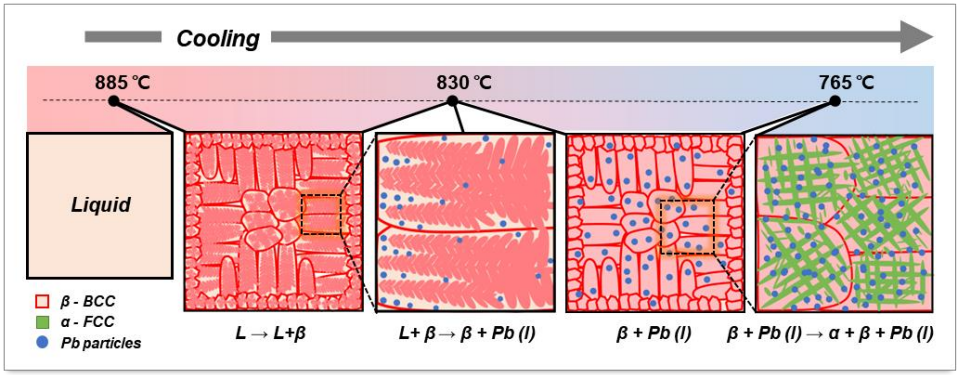

Figure 3.4 Schematic descriptions of the microstructural evolution during the solidification and phase transformation of as-cast $Cu_{58}Zn_{39}Pb_3$ wt.% alloy

solidification and phase transformation in the as-cast $Cu_{58}Zn_{39}Pb_3$ leaded-brass alloy of this study. The temperature in the below diagram is based on equilibrium, and the β phase is formed in the liquid when the as-cast $Cu_{58}Zn_{39}Pb_3$ alloy passes approximately 885 ℃ during the cooling process. As shown in Figure 3.5, it is formed of chill zone, columnar zone, and equiaxed zone. In general, the macrostructure of an ingot is composed of these three zones. [28] The columnar zone was formed from β-phase dendrites surrounded and α-phase interdendrite around it, and the dendritic arm appeared to be several tens of μm. [29, 30] As the composition of the residual liquid, which is 10% based on the equilibrium phase diagram and 15% based on the non-equilibrium phase diagram, Figure 18, approaches Pb 20 wt.%, it can be seen that phase transition from single β + Pb(l) to β + α + Pb by monotectic reaction as shown in Figure 3.6(a). Then, a phase change from β to α + β occurs and belong to the duplex brass region. Since the microstructure is formed by the above process, the Pb particle content is quite high in the liquid part that is solidified at the end. Figure 3.7 compares the distribution of Pb particles through OM, SEM-BSE, and EDS mapping images observed for the center, $\frac{1}{4}$ position, and edge parts of the cross section of $Cu_{58}Zn_{39}Pb_3$ leaded-brass alloy as-cast specimen. As a result, the content of Pb particle was 4.7% at the center, 2.8% at the quarter position, and 2.4% at the edge, confirming that the non-uniform distribution and heterogeneity of Pb particles was high in the as-cast sample, and the content of Pb particle was high at the center.

The microstructure of these as-cast specimens changes through a hot extrusion process. In Figure 3.8, the microstructure of the specimen corresponding to the

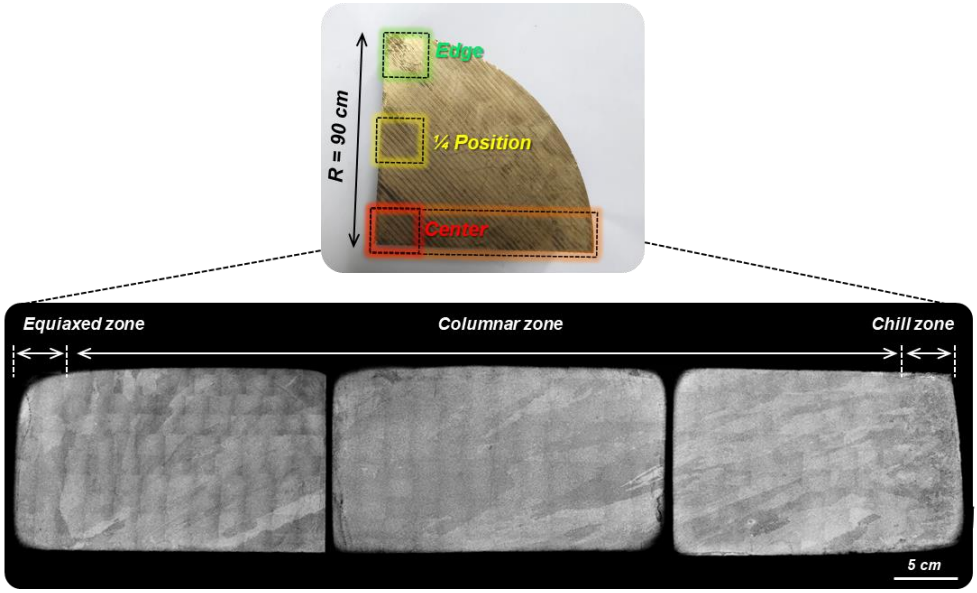

Figure 3.5 Photo of quadrant of the cross-section of an as-cast $Cu_{58}Zn_{39}Pb_3$ wt.% alloy and the corresponding optical microscope image showing chill zone, columnar zone, and equiaxed zone

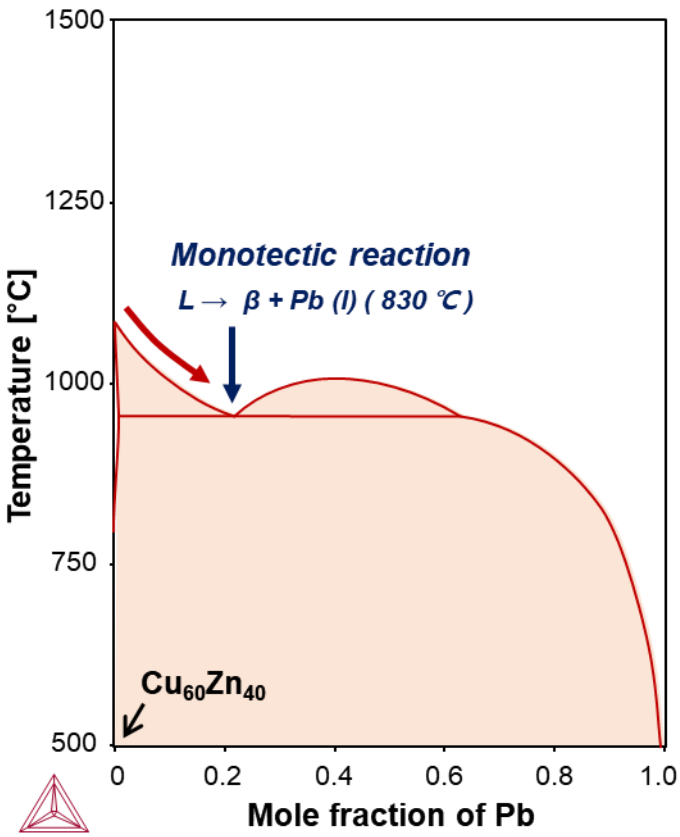

Figure 3.6 Pseudo binary phase diagram of ($Cu_{60}Zn_{40}$) - Pb alloy system calculated by Thermo-Calc software using SSOL6 database.

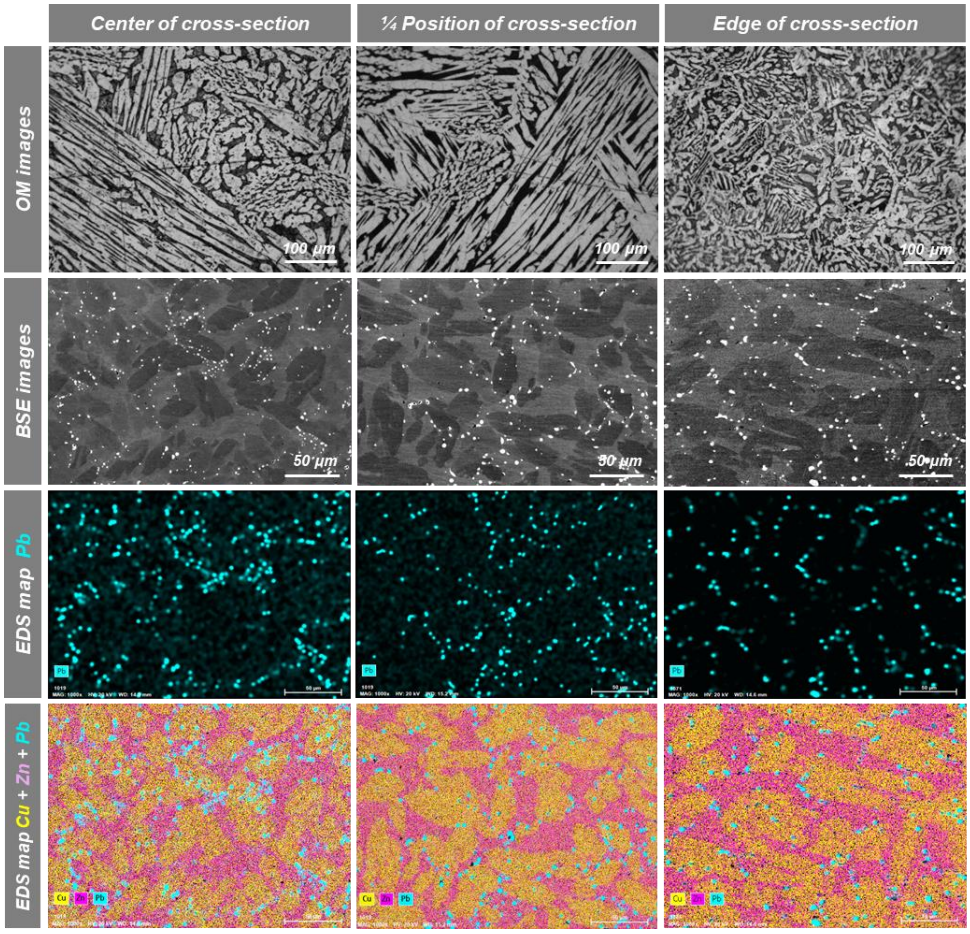

Figure 3.7 Optical microscope images, SEM images obtained using backscattered electron detector, and energy dispersive spectroscopy maps obtained from the center, ¼ position, and edge of cross-section of as-cast $Cu_{58}Zn_{39}Pb_3$ wt.% alloy; ¼ position indicates a position at a distance of d/4 from the center of the cross-section

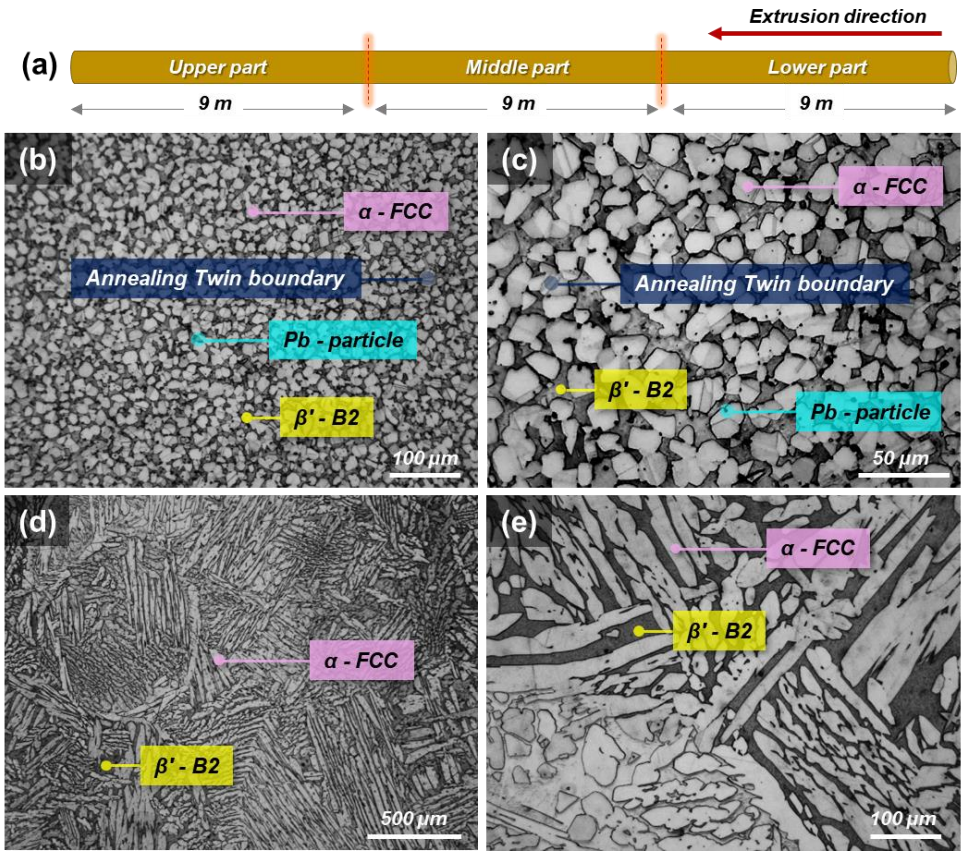

Figure 3.8 (a) A schematic description showing the upper, middle, and lower part of extrudates, Optical microscope images of middle part of hot-extruded (b),(c) $Cu_{58}Zn_{39}Pb_3$ wt.% alloy and (d),(e) lead-free $Cu_{60}Zn_{40}$ wt.% brass alloy at 730 °C

extrusion at 730 ℃ was observed through OM. (a) and (b) are for the $Cu_{58}Zn_{39}Pb_3$ leaded-brass alloy, and (c) and (d) are for the $Cu_{60}Zn_{40}$ lead-free brass alloy. As a result, Pb particles were distributed in FCC/BCC boundary and FCC annealing twin boundary in hot extruded leaded-brass to form a uniform isotropic blocky structure. This showed that Pb particle acts as a nucleation site and FCC phase growth inhibitor. It is known that the α-β' interphase boundary, which has a higher surface energy compared to the α-α and β'-β' boundaries, is the preferred site for the nucleation of Pb particles. [11] The hot-extruded lead-free brass alloys shown in (c) and (d) were formed with a $Widmanstätten$ structure due to the absence of such a microstructure controlling factor.

Alloys with columnar structures decrease the ductility and formability because strain transfer between grains is suppressed during plastic deformation. Great efforts are required to prevent the formation of directional columnar structures and coarse grains during solidification, including alloying additives for equiaxed grains and inoculant treatment for refined grains. [13] When using the alloy in this as-cast form, the formation of columnar grains should be avoided in order to increase workability and reduce mechanical anisotropy. [13]

3.2. Effect of Pb on microstructure of brass alloy($Cu_{58}Zn_{39}Pb_3$ wt.%)

Pb has no solubility in Cu and Zn, so it precipitates in interdendritic regions or grain boundaries. [3, 29] In the as-cast state of leaded-brass alloy, Pb is non-uniformly distributed, and this segregation promotes constitutional supercooling to form dendrite. [29] The nuclei of equiaxed grains are formed during solidification in a supercooled liquid away from the interface of different phases due to compositional fluctuations of the melt or convection of the nuclei generated in the chill zone of the dendritic arms. [13] The driving force for nucleation mainly comes from thermal supercooling and compositional supercooling. [13]

The role of Pb in leaded-brass can be divided into three major categories: inhibition of α phase growth, function as a nucleation site and reduction of grain size. First, the annealing twin boundary generally has a low surface energy, and most of these particles remained at the grain boundary during grain growth with little particle precipitation inside the grain. This behavior was interpreted as the particles being dragged by grain boundary migration, providing evidence for the slow growth of α grains.

Second, the Pb particle is located near the annealing twin, suggesting that the Pb particle might be the nucleation site of annealing twins. [11]

Thirdly, Pb reduces the grain size in brass alloys. [29] In addition, the size and distribution of the Pb globule affect the machinability of the material, and it is known that smaller and better dispersed Pb particles promote better machinability. [9]

In addition, fine and uniform lead distribution leads to less wear and better chip

fracturing, facilitating the machining process, while excessive lead or non-uniform lead distribution can cause surface cracks due to hot shortness during hot working, therefore Pb needs to be uniformly distributed. [13]

The distribution of Pb globules is not affected by the extrusion process because Pb is completely insoluble in copper and precipitates at the end of the solidification process, and since lead precipitates at the end of solidification, their size and distribution are mainly affected by casting and solidification conditions. [10, 15] When Pb is not sufficiently dispersed in the microstructure and too large Pb globules are present, bad cutting-saw behavior and high tool wear result. [10] The most proper way to obtain a smaller and better dispersed Pb globule distribution is to use a higher cooling rate after solidification. [10]

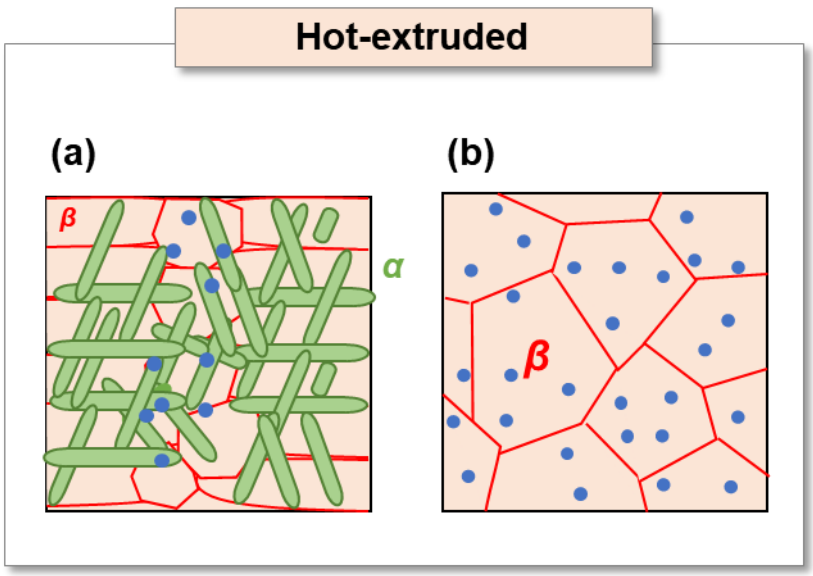

Figure 3.9 Schematics of microstructure modifications and Pb distribution during hot-extrusion (a) hot-extruded at $\alpha + \beta$ phase region and (b) hot-extruded at single β phase region

3.3. Summary

Pb is not soluble in Cu-Zn alloys and globular Pb formation appears at interdendritic region or grain boundary.($T_{m,Pb} = 327.5$ ℃)

In the case of as-cast, liquid melting is perfomed at a high temperature of 1070 ℃, and therefore Pb particles are heterogeneously distributed due to high convection of liquid melts. Heterogeneous nucleation occurs at the surface in contact with the mold. Also, dendritic β-phase is formed from constitutional supercooling.

In the case of the hot extrusion process, it was confirmed that the globular shape of Pb was formed at the α/β boundary when the heat treatment proceeded in the single β region(T > 765 ℃). This will be explained in more detail in Chapter 4.

In the leaded-brass extrudate, there are three effects of Pb on microstructure of brass alloy, growth resistance factor of α-phase, nucleation site of α-phase, and reducing the grain size. In addition, it is preferable to uniformly disperse small-sized lead in terms of improving machinability, and for this purpose, a fast cooling rate after solidification can be applied.

As a result of confirming the distribution of the Pb particles in the microstructure, Pb particles also exist inside the β and α phases in the as-cast sample, and at the α/β phase boundary or annealing twin boundary of α-FCC in the hot-extruded sample.

CHAPTER 4

Structural heterogeneity induced by extrusion condition

4.1. Extrusion temperature and position of sample

In evaluating the excellent machinability of specimens after hot-extrusion, in this paper, (1) formation of uniform isotropic structure, (2) fraction of β' phase, (3) grain size of α-FCC phase, (4) uniformity of Pb distribution, which serves as a lubricant during cutting are the main factors the analysis was focused on.

In order to analyze the impact on microstructure and mechanical properties in the extrusion process, two variables were systematically varied. The experimental inveestigation involved the preparation of a total of six sample conditions, achieved by considering two different extrusion temperatures and three distinct specimen positions within a 27m rod-shaped extruded material(also called extrudate). [23] Hot extrusion involves heating the metal material to temperatures above its recystallization point, and the temperature range is typically expressed as a percentage of the material's melting point. In the case of copper and aluminium alloys, the industry commonly emplys a heating temperature range of 0.75 to 0.9 times the melting point of the alloy when producing extruded materials. In this research, the $Cu_{58}Zn_{39}Pb_3$ leaded-brass alloy specimen underwent thermal analysis using NETZSCH DSC, and the melting point was determined to be 882.23 ℃ as shown in Figure 4.1. As a result, the tmeperature range corresponding

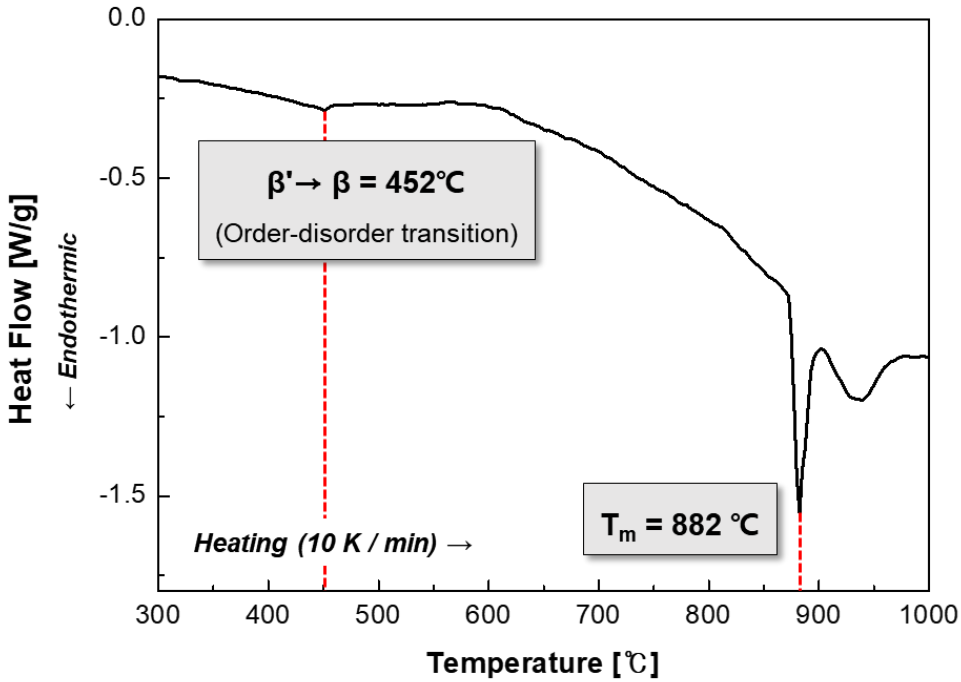

Figure 4.1 DSC curve of $Cu_{58}Zn_{39}Pb_3$ wt.% alloy with the heating rate of 10 K/min

to 0.75 T_m to 0.9 T_m was approximately 670 ℃ to 790 ℃. In general, the upper limit of the extrusion temperature is set to be at least 100 ℃ below the melting point of the alloy. [31] While hot-working offers the advantage of reducing flow stress, it introduces certain challenges associated with elevaed temperatures, including (a) Oxidation of the billet and extrusion tools, (b) Softening of the die and tools, (c) Difficulties in providing sufficient lubrication, and (d) The potential for burning of hot shortness when extensive deformation occurs during extrusion due to the generation of significant internal heat. [23] Considering these issues, it is beneficial to employ the lowest possible working temperature that still provides adequate plasticity to the metal. [23] Moreover, cost considerations also play a role in the decision-making process. [23] Defections impacting the quality of extruded products may arise based on material and processing conditions. Elevated temperatures or high extrusion speeds and friction can lead to increased surface temperature, causing surface cracks and tearing. Similarly, low temperatures may induce surface cracks due to periodic material condensation on the die. Additionally, excessive extrusion temperature, friction, and speed can significantly elevate surface temperature and cause surface cracks, while too low temperatures can also result in surface cracks. Furthermore, in products requiring substantial strength, the extruded part at the tip, which is subjected to relatively lower extrusion pressure and has lower strength compared to other parts, may be more prone to failure upon initial usage after extrusion. Therefore, determining the feasible extrusion temperature range for the specific material in the extrusion process and identifying the minimum temperature that exhibits excellent physical properties are essential steps in process optimization. Therefore, in this study, the potential hot extrusion temperature range for the

$Cu_{58}Zn_{39}Pb_3$ leaded-brass alloy was considered to be 670 ~ 780 ℃. Subsequently, after preheating the billet to 700 ℃ in the heating furnace, the extrusion temperature was set at 670 ℃(lower limit temperature), with a 30 ℃ reduction based on the preheated billet, and 730 ℃(upper limit temperature), with a 30 ℃ increase, to conduct the extrusion process.

Some limitations of the extrusion process are that extrusion generates higher process waste compared to rolling, with approximately 10 ~ 15% waste in extrusion, whereas rolling results in only 1 ~ 3% waste. [23] Since the extrusion waste comprises an extruded butt(discard) and a leading end of the extruded product with insignificant deformation. [23] In this research, a 27m length extruded rod of $Cu_{58}Zn_{39}Pb_3$ leaded-brass alloy was produced by reducing a billet with a diameter of 180mm to 20mm, resulting in an 88.9% reduction, as described earlier. Therefore, in this study, to investigate the positional influence on the extensively long extruded rod of 27m, three distinct sections of the specimen were prepared: the upper part for the initially extruded material, the middle part for the intermediate extruded material, and the lower part for the material extruded at the end. Throughout this paper, the designations 'Upper part of extruded product', 'Middle part of extruded product', and 'Lower part of extruded product' will be denoted as 'upper', 'middle', and 'lower', respectively. Additionally, in the radial direction, it was divided into 'center', '$\frac{1}{4}$ position', and the 'edge' of the cross-section as illustrated in the figure 3.5

4.2 Longitudinal direction analysis of hot extruded $Cu_{58}Zn_{39}Pb_3$ wt.%

4.2.1 Microstructural analysis

The microstructures of the upper, middle, and lower were compared to confirm the structural heterogeneity of the extrudate in the longitudinal direction. The Figure 4.2 is an OM image of the microstructure observed at the center of a quadrant for each condition of hot extrusion temperature at 670 °C and 730 °C. In order to assess the uniformity in the direction of hot extrusion, which is the longitudinal direction, precise analyses were performed for all parts, including the upper, middle, and lower parts.

According to the four key perspectives mentioned in Section 4.1, a microstructural analysis was conducted. Firstly, the α-FCC phase size was examined for each extrusion condition, with particular attention to the evolution of the Widmanstätten structure in the as-cast alloy. As depicted in Figure 4.2, the upper and middle parts extruded at 670 ℃ exhibited the Widmanstätten structure, while the α phase in the lower part at 670 ℃ and the samples at 730 ℃ appeared as isotropic blocky structures. The obtained Widmanstätten structure of the α phase could be attributed to its influence from the as-cast samples.

The thermodynamic calculations conducted with the results, indicating that the $\alpha + \beta$ duplex region occurred below 765 ℃, as shown in Figure 2.2(b) and Table 1. During the hot working of duplex brass, an increase in the degree of deformation leads to formation of the strain localization. [31] In the hot extrusion process of duplex brass, the differing flow stresses of the α and β phases, can induce stress

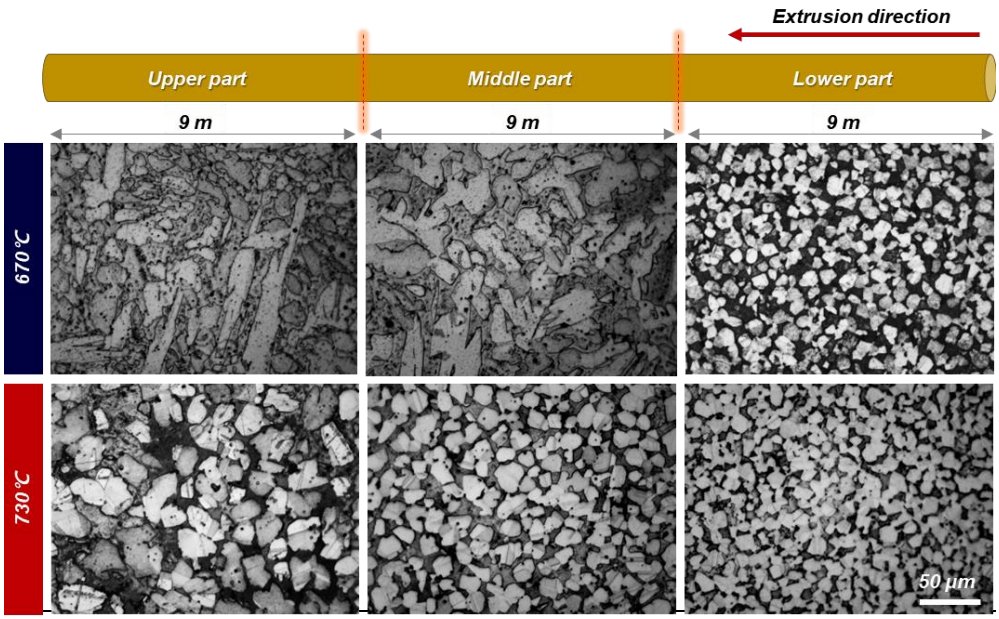

Figure 4.2 Optical microscope images obtained from upper, middle, and lower part of hot-extruded $Cu_{58}Zn_{39}Pb_3$ wt.% alloy at 670 ℃ and 730 ℃

and strain localization, thereby promoting dynamic recrystallization predominantly within the region of strain localization. [25, 31, 32] This phenomenon plays a crucial role in determining the final microstructure of the extrudate.

In contrast, the lower part extruded at 670 °C and the specimens extruded at 730 °C reveal that the actual extrusion process occurred within the single β phase region, which exists above 765 °C. Unlike the leaded-brass alloy, the lead-free brass alloy exhibits the as shown in Figure 3.8 (d) and (e) The isotropic blocky α-FCC phase of the hot-extruded $Cu_{58}Zn_{42}Pb_3$ wt.% alloy can be attributed to two main factors.

First, after dynamic recrystallization, during the subsequent static recrystallization, the dislocation cell structure plays an influential role as a preferred nucleation sites for the formation of β phase withinthe single β phase region. In addition, as a preferredn nucleation site for phase formation in a single β phase region, uniformly distributed immiscible Pb particles act as a factor to inhibit grain growth. As the nucleation site of α phases tends to dominate at the refined grain boundaries of the β phase, a constant α phase fraction results in a reduction in the distance between preferred nucleation sites, leading to a decrease in the aspect ratio of α phase.

Furthermore, the second, during the phase transformation from β to $\alpha + \beta$, Pb particles preferentially occupy α/β boundaries, leading to a reduction in the mobility difference between incoherent and coherent interfaces. [21] Notably, despite setting the extrusion temperature below the single β phase region, the actual extrusion occurred within the β phase region. This occurrence can be attributed to two primary factors associated with direct extrusion : (i) the frictional heat generated between the ingot and the mold and (ii) the heat generated by plastic

deformation, resulting in an increase in temperature during the extrusion process. [25, 33, 34]

Obtaining continuous and quantitative temperature measurements for all positions presents challenges due to temperature variations along the upper, middle, and lower parts. By analyzing the microstructure of the lower part extruded at 670 ℃, it becomes evident that a substantial temperature rise of more than 100 ℃ occurred in specimens commonly employed in industrial applications. Previous studies have shown that the formation of Widmanstätten structures can result in irregularities and anisotropic features in the microstructure and it leads to stress concentration and shear localization, giving rise to void and crack formation during machining processes. [35-37] Consequently, the upper and middle parts extruded at 670 ℃ are anticipated to have relatively lilmited machinability, whereas the lower part extruded at 670 ℃ and the specimens extruded at 730 ℃ are expected to demonstrate improved machinability.

The second aspect to focus on with regard to microstructural analysis was the fraction of the β'-B2 phase. Since the β' phase has high hardness and brittleness, increasing the fraction of the beta phase generally improves machinability. However, defining a quantitatively optimum fraction is challenging due to the synergistic interaction between the size and morphology of the α phase and β' phase fraction. Previous studies often consider an approximate range of 20% to 40% of β' phase fraction as favorable for good machinability. Fig. 4.3(a) presents the β’ fraction for each analyzed extrusion condition based on micrographs, showing variations ranging from 28.8% to 47.7% depending on the extrusion temperature and position. The cause of the β'-phase fraction variation observed under each extrusion condition was

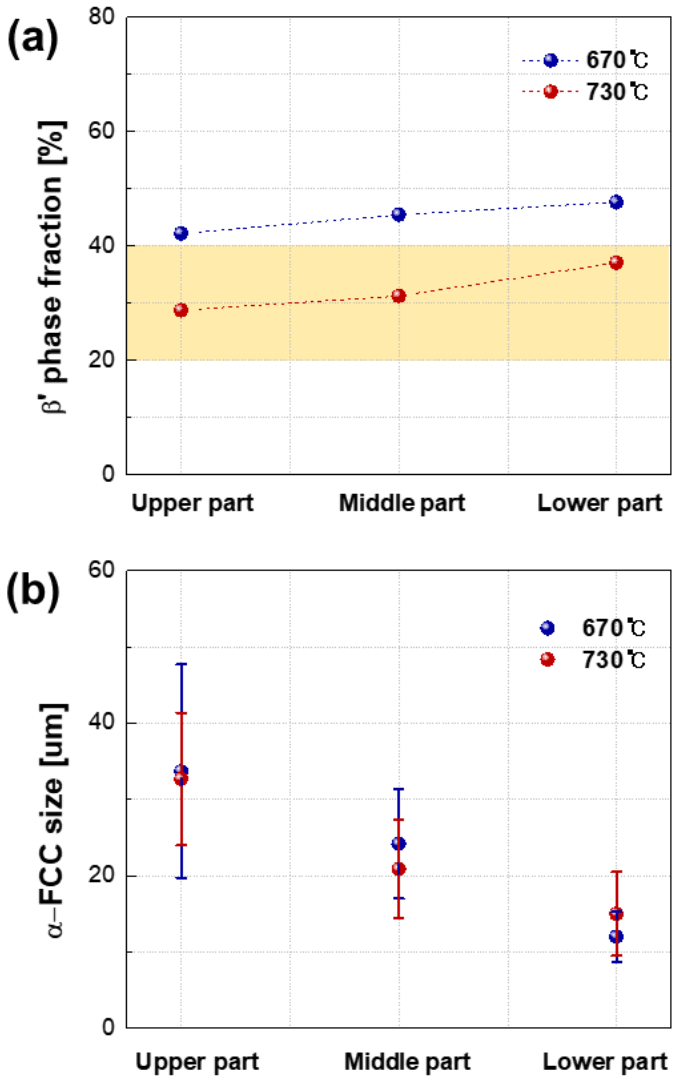

Figure 4.3 (a) β'-B2 phase fraction and (b) α-FCC size of upper, middle, and lower part of hot-extruded $Cu_{58}Zn_{39}Pb_3$ wt.% alloy at 670 ℃ and 730 ℃

β' phase fraction	Upper part	Middle part	Lower part
Extruded at **670** ℃	42.2%	45.5%	47.7%
Extruded at **730** ℃	28.8%	31.3%	37.1%

Table 4.1. β'-B2 phase fraction of upper, middle, and lower part of hot-extruded $Cu_{58}Zn_{39}Pb_3$ wt.% alloy at 670 ℃ and 730 ℃

investigated. The fraction of the β'-phase is significantly impacted by both the extrusion temperature and the die force. [24, 25, 31] Since extrusion temperature and die force variations occur simultaneously when comparing different positions, these two factors can mutually influence each other. Given the intricacies and constraints in determining the origin of the β'-phase fraction, our primary focus was on explaining the temperature-based distinctions at the same position. Our observations align with prior research, indicating that the β'-phase fraction decreases with an increase in extrusion temperature at the same position. [24, 38] In the upper, middle, and lower parts of the specimen extruded at 670 °C, the β'-phase fractions were measured as 42.2%, 45.5%, and 47.7%, respectively as shown in Table 4.1. For the specimens extruded at 730 °C, the corresponding β'-phase fractions were 28.8%, 31.3%, and 37.1%, indicating reductions of 31.8%, 31.2%, and 22.2%, respectively, compared to those at 670 °C. This trend can be explained by considering the change in die force and plastic deformation with varying extrusion temperatures. At the sample position, higher extrusion temperatures result in lower flow stress and reduced plastic deformation at the same extrusion speed, leading to a relatively lower dislocation density in materials extruded at higher temperatures and consequently a lower driving force for the phase transformation from β phase to (α + β) phases after extrusion. [24, 25] As a consequence, materials extruded at high temperatures display comparatively reduced dislocation densities, leading to a diminished driving force for the phase transformation from β phase to (α+β) phase following the extrusion process. While there are limitations in quantitatively analyzing the non-equilibrium phase transformation during continuous cooling, it is inferred that the phase transformation from β to (α + β) phases occurs at lower temperatures. Some

previous investigations have referred to this phenomenon as stress-indeuced phase transformation, which correlates with a lower β phase fraction at lower extrusion temperatures. [24, 25]

The subsequent investigation focused on the variation of the β-phase fraction according to the position under identical extrusion temperature conditions. For both extrusion temperatures, an upward trend in β phase content was observed from the upper part to the lower part, despite the lower extrusion temperature at the lower part. This phenomenon can be attributed to the rise in deformation load towards the lower part, arising from a combination of decreased inserted billet temperature and increased friction load, resulting in severe plastic deformation. [23-25] Hence, similar to the previously discussed phenomenon, the elevated dislocation density contributes to the increased β phase fraction, referring that the β → (α + β) phase transformation is finished at relatively higher temperatures. Considering the comprehensive results, an extrusion temperature of 730 ℃ was found to have a β-phase fraction within the range of 20% to 40% with better machinability. Consequently, an extrusion temperature of 730 ℃ is expected to be more suitable for achieving cutting performance and superior machinability compared to 670 ℃.

Thirdly, we focused on the grain sieze of the α-FCC phase, and the results shown in Fig. 4.3(b) followed the ASTM E1382 determining average grain size measuremen method. [39, 40] The ASTM standard E1382 provides a measurement procedure using the linear intercept length method, which is validated for base material microstructures. [41] The influence of grain size distribution on the mechanical properties of engineering materials is significant, prompting the need for improved guidelines for measuring grain size distribution in various industrial

materials. [42] The properties of metallic products often depend on the grain size and distribution of their microstructures. [42] To ensure consistent material properties and establish a connection between processing and structure, standardized measurement methods for microstructure are essential. [42] Widely accepted standards like E1382 is employed for measuring the average grain size in both single and multiphase materials. [42] The α-FCC sizes of the upper, middle, and lower of the specimen hot-extruded at 670 ℃ were measured as 33.7 ± 14 μm, 24.2 ± 7.2 μm, and 12 ± 3.2 μm respectively. Here, the upper and middle parts contain an anisotropic Widmanstätten structure, so the standard deviation is larger than that of the lower part containing of an isotropic blocky structure. Meanwhile, in the case of the 730 ℃ extruded specimen, the α-FCC sizes were measured as 32.7 ± 8.7 μm, 20.9 ± 6.4 μm, and 15 ± 5.5 μm from the top to the bottom, respectively. In both hot extrusion temperatures, the size of the α phase gradually diminishes towards the lower part. The observed phenomenon can be ascribed to a synergy of factors, encompassing a decrease in the temperature of the inserted billet and an increase in the friction load, leading to higher deformation load in the lower part. [23-25] Consequently, the lower part experiences more severe plastic deformation, leading to the formation of a more intense dislocation cell structure, which acts as a nucleation site for the β phase during static recystallization. As a consequence of the decreasing size of the β phase, the α phase, which nucleates at the β/β grain boundaries during phase transformation, also reveals a reduced size towards the lower part.

Comparing the extrusion temperatures at each position, it is difficult to directly compare the size of the α phase, primarily due to the morphological distinctions of

the α phase contingent upon whether extrusion occurred in the (α + β) region or the single β region. Notably, in the lower part, where more severe plastic deformation takes place at a lower extrusion temperature due to increased deformation load, a reduction of approximately 20% in the size of the α phase is observed. As there is no definitive criterion for the optimal size range of the α phase to achieve favorable machinability, the subsequent section will investigate the impact of α phase size on machinability based on the assessment of mechanical properties, which are influenced by the combination of the size of the α phase and the phase fraction of the β phase.

Fourth, in the last part of microstructural analysis, we conducted an assessment for the uniformity of Pb particle distribution, forming a thin film on the chip's side that slides against the contact with the tool, functioning as a lubricant during machining. [8, 38, 43] Notably, our observations revealed a non-uniform distiribution of Pb particles in the as-cast alloy, known to contribute to surface cracking. [38, 44, 45] Consequently, we focused on investigating whether Pb particles exhibited a uniform distribution folllowing hot extrusion. [38, 44, 45] Furthermore, considering that the coalescence of Pb particles leads to an increase in mean particle diameter and a decrease in population density, adversely impacting machinability, we also conducted a meticulous analysis of the size of Pb particles. Fig 4.4 displays SEM images and EDS maps of the upper part of the 670 ℃ extrusion and the lower part of the at 730 ℃ extrusion, corresponding the Widmanstätten structure and the blocky structure, respectively. The EDS maps represent the elements Cu, Zn, and Pb by yellow, pink, and sky blue colors, respectively. By analyzing the 60 μm × 60 μm regions represented by dashed lines in each specimen, we compared the uniformity

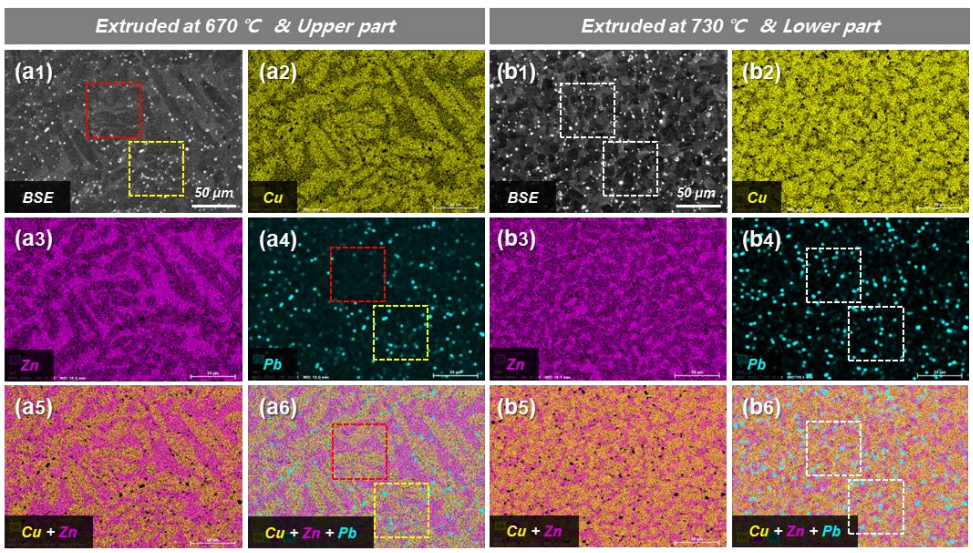

Figure 4.4. SEM images obtained using backscattered electron detector and energy dispersive spectroscopy maps obtained from (a1)-(a5) upper part of hot-extruded $Cu_{58}Zn_{39}Pb_3$ wt.% alloy at 670 ℃ and (b1)-(b5) lower part of hot-extruded $Cu_{58}Zn_{39}Pb_3$ wt.% alloy at 730 ℃. EDS maps show the distribution of elements Cu (yellow), Zn (pink), and Pb (sky blue), respectively

of Pb particle distribution. As a result, in the upper part extruded at 670 ℃, the red dashed area indicates a sparse distribution of Pb particles, while the yellow dashed area represents a more abundant distribution of Pb particles. Conversely, in the lower part extruded at 730 ℃, the white dashed area signifies a uniform distribution of Pb particles throughout the entire specimen. Additionally, the average size of Pb particles was approximately 1.5 ± 0.2 μm in both specimens, and there was no significant difference observed between the two. In the specimen where extrusion conducted in the α + β region, the distinct flow stress of each phase led to strain localization ,acting as the primary nucleation site for recrystallization. Furthermore, in the inhomogeneous (α + β) brass alloy, the flow pattern 'C' is observed and it leads to a relatively non-uniform distribution of Pb particles in this specimen. [23] In contrast, specimens hot extruded within the single β region do not experience stress and strain localization, enabling uniform dynamic and static recrystallization. In addition, during the hot extrusion of the uniform β-brass alloy, flow pattern 'B' is observed, leading to internal redistribution of particles and consequent uniform distribution of Pb particles. [23, 25, 31] Considering the significance of a uniform distribution of Pb particles for machining, as it improves chip fracturing and minimizes tool wear, it can be deduced that the extrusion temperature of 730 ℃ is more optimal. Based on the various evaluation factors of microstructure mentioned above, it can be deduced that the upper part and middle part extruded at 670 ℃ are likely to demonstrate comparatively inferior machinability. Conversely, it is anticipated that the lower part extruded at 670 ℃ and the specimens extruded at 730 ℃ would exhibit excellent machinability.

4.2.2 Mechanical analysis

The representative specimens selected for evaluation were consisted of the upper part extruded at 670 ℃ with a Widmanstätten structure and the lower part extruded at 730 ℃ with a blocky structure. Uniaxial tensile tests were performed on each specimen to assess their mechanical properties. To enable a comparison between the free-cutting leaded brass alloys and the lead-free brass alloy, uniaxial tensile tests were also conducted on the Cu60Zn40 wt.% alloy, hot-extruded at 730 ℃, as depicted in Fig. 3.8 (c) and (d). Fig. 4.5 presents the uniaxial tensile stress-strain curves for the hot-extruded Cu60Zn40 wt.% alloy at 730 ℃, and the Cu58Zn39Pb3 wt.% alloy hot-extruded at 670 ℃ and 730 ℃, marked by green, sky blue, and red solid lines, respectively. The results show a notable 31.6% increase in yield strength for the 670 ℃ extruded upper part compared to the lead-free brass alloy. Furthermore, the 730 ℃ extruded lower part exhibits a significant 22.8% higher yield strength in comparison with the 670 ℃ extruded upper part. On the contrary, the strain to fracture decreases by 11.0% for the 670 ℃ extruded upper part and 21.2% for the 730 ℃ extruded lower part, respectively. These enhancements in yield strength for each extruded specimen are attributed to their respective microstructures. It is worth noting that Pb particles do not exert a significant influence on the strength and ductility. [46] Therefore, our focus was primarily on the phase fraction of α and β phases, as well as the grain size of each phase. To perform a quantitative analysis, we interpreted the mechanical properties based on calculations utilizing the extended Hall-Petch relation. Specifically, we used the extended Hall-Petch relation, an extension of the traditional Hall-Petch relation, to characterize the dual-phase brass

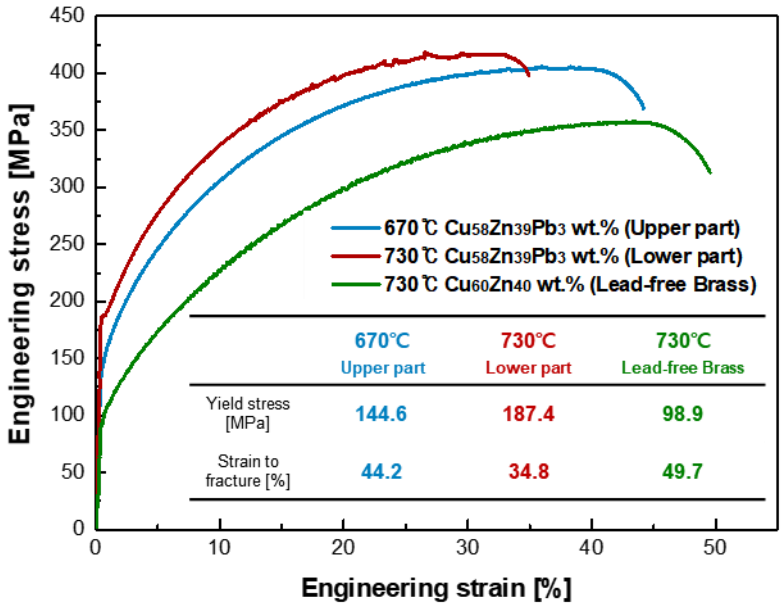

Figure 4.5. Uniaxial tensile stress-strain curves for hot-extruded $Cu_{60}Zn_{40}$ wt.% at 730 ℃ (green), and hot-extruded $Cu_{58}Zn_{39}Pb_3$ wt.% alloy at 670 ℃ (sky blue) and 730 ℃ (red), respectively

alloy. It is considered that on the basis of the dislocation pile-up theory, the phase boundary between α and β phases and the prior β/β grain boundary serve as hindrances to dislocation movement. [39, 40, 47, 48] The proposed simplified extended Hall-Petch equation is given as follows [47]:

$$\sigma_y^c = \sigma_y^{0c} + k_y^c \cdot \bar{d}^{-1/2} \tag{4.1}$$

where $\sigma_y^c, \sigma_y^{0c}, k_y^c$ are the yield strength, lattice friction stress, and the Hall-Petch coefficient of dual phase brass alloy, respectively.

$$\bar{d} = d_\alpha f_\alpha + d_\beta f_\beta \tag{4.2}$$

$\bar{d}$ value is a volume fraction weighted average grain size. d_α, d_β are the grain size of each phases and f_α, f_β are phase fractions of α and β phase, respectively. Based on the β phase fraction, σ_y^{0c} is experimentally investigated in the previous studies. Therefore, the σ_y^{0c} values 44, 50, 48 MPa for 730 ℃ extruded lead-free alloy, 670 ℃ extruded upper part, and 730 ℃ extruded lower part, respectively were used in this research. [40, 47] The k_y^c also exhibits a significant dependence on the β phase fraction, and the respective values are 13.8, 13.9, 14.1 $\text{MPa} \cdot \text{mm}^{1/2}$. The $\bar{d}$ values were determined through calculations involving the phase fraction and measured intercept length of α and β phase regions, following the guidelines outlined in ASTM E1382, resulting in values of 65 μm, 30 μm, and 12.6 μm for the three cases, respectively. Based on each factor, the calculated σ_y^c values were 98.1 MPa, 130.2 MPa, and 173.4 MPa for the lead-free brass alloy hot-extruded at 730 ℃, the upper part of hot-extruded at 670 ℃, and the lower part of hot-extruded at 730 ℃, respectively. These calculated values exhibit a similar trend to the measured values. Therefore, the observed enhancement in yield strength for each specimen can be

definitely explained by differences in their phase fractions and $\bar{d}$, the volume fraction weighted average grain sizes, as depicted in Fig. 4.6. The figure indicates the contributions of lattice friction stress, shown in the gray area, and phase boundary strengthening, represented by the colored area, to the yield strength of each specimen. Notably, despite the differences in the beta phase fraction among the samples, being 31.8%, 42.2%, and 37.1%, it becomes evident that the primary factor influencing the results is the phase boundary strengthening effect, rather than the variation in the σ_y^{0c} values.

It is challenging to quantitatively predict machinability only with mechanical properties, but machining factors also play an important role in determining machinability for duplex brass alloys. In general, it is known that, alloys with higher strength tend to be preferred since it forms chips more easily and minimizes tool wear, resulting in excellent machinability. [2, 16, 38, 49] According to the reference, the composition of Cu58Zn39Pb3 wt.% alloy, commonly used in the industry, indicates a yield strength of approximately 200 Mpa. [16] Consequently, it is expected that the 670 ℃ extruded upper part, with lower strength, would demonstrate relatively poor machinability. Conversely, the 730 ℃ extruded lower part, characterized by increased strength and reduced ductility, is expected to be classified as a similar free-cutting level in the machinability test through the section 4.4.

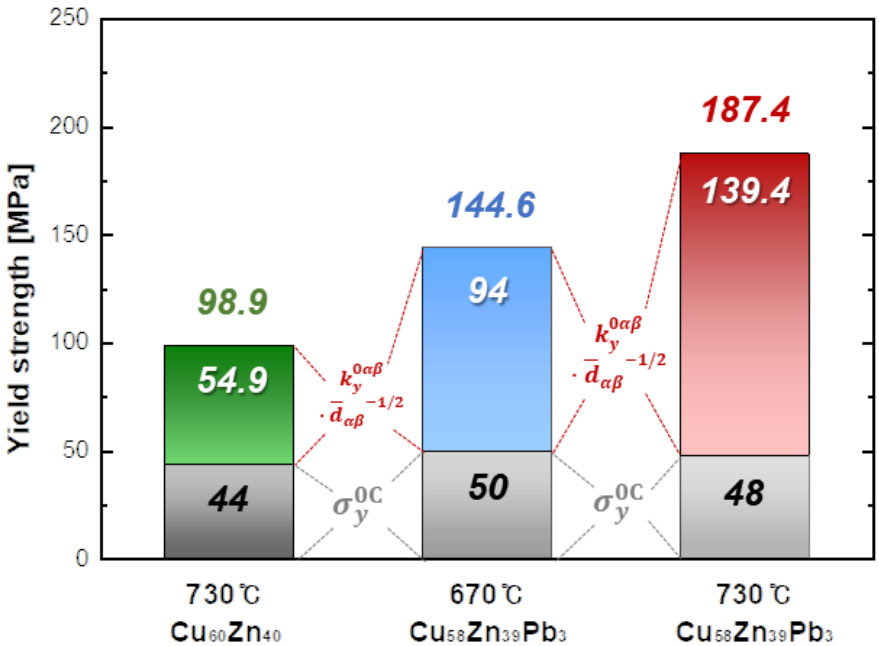

Figure 4.6. The contribution of lattice friction (gray) and phase boundary strengthening to the yield strength of hot-extruded $Cu_{60}Zn_{40}$ wt.% at 730 ℃ (green), hot-extruded $Cu_{58}Zn_{39}Pb_3$ wt.% at 670 ℃ (sky blue) and 730 ℃ (red)

4.3. Radial direction analysis of hot extruded $Cu_{58}Zn_{39}Pb_3$ wt.%

4.3.1 Microstructural analysis

After evaluating the variation along the extrusion direction, that is, the longitudinal direction of the specimen in the previous section, this section focuses on the homogeneity assessment by each temperature and position in the cross sections perpendicular to the extrusion direction. Specifically, a detailed examination of micrographs was conducted for both the center and edge regions of the cross-sections. Additionally, we assessed the overall homogeneity of each condition's cross-section by conducting continuous hardness scanning from the center to the edge. The overall microstructure of the quadrant cross-section of each specimen obtained from the upper, middle, and lower parts of the hot-extruded specimens at 670 °C and 730 °C is shown in Fig. 4.7. Fig. 4.8 shows OM images captured from the center and edge of the cross-sections obtained from the above specimens. Figure 4.8 reveals that the upper and middle parts extruded at 670℃ exhibit the presence of the Widmanstätten structure at both the center and edge, consistent with the representative image Fig. 4.2 depicted in section 4.2. As shown in Figure 4.8, 42.1 ± 34.6 μm, 32.8 ± 16.6 μm, 36.8 ± 15.9 μm, and 27.3 ± 12.1 μm were measured at the center and edge of the upper and middle parts specimens extruded at 670 ℃, respectively. Based on these findings, it is evident that the size of the α-phase diminishes towards the edge. In direct extrusion, as opposed to indirect extrusion, the friction between the billet

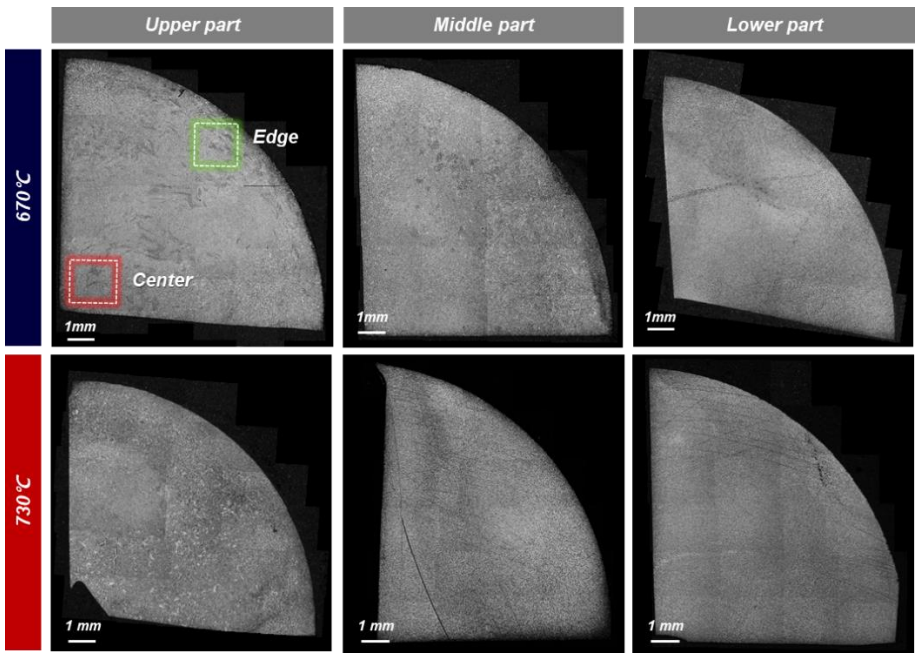

Figure 4.7 Optical microscope images of quadrant cross-section obtained from upper, middle, and lower parts of hot-extruded $Cu_{58}Zn_{39}Pb_3$ wt.% alloy at 670 °C and 730 °C

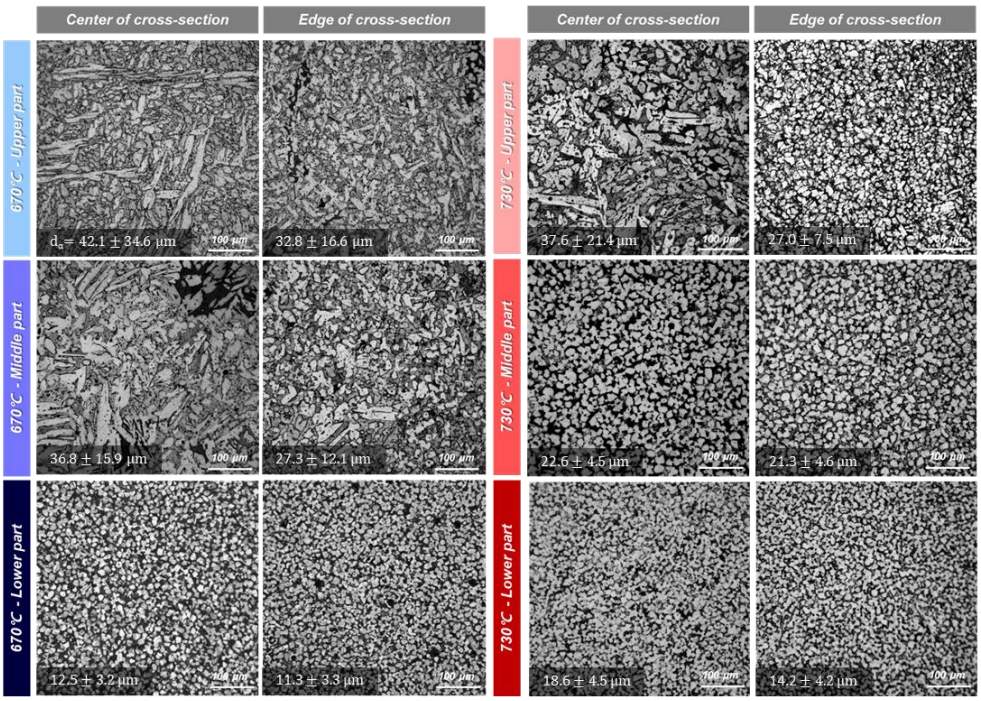

Figure 4.8 Optical microscope images of center and edge of cross-section obtained from upper, middle, and lower parts of hot-extruded $Cu_{58}Zn_{39}Pb_3$ wt.% alloy at 670 °C and 730 °C. d_α indicates the average size of α-FCC phase

and mold rises from the center to the edge of the cross-section, inducing a severe plastic deformation. Consequently, an increased number of nucleation sites arise, leading to a reduction in the size of the α-phase towards the edge. Additionally, during the cooling process, the edge undergoes a relatively higher cooling rate, inhibiting the growth of the α phase, leading to a relatively smaller α phase size in comparison with the center. In the case of the lower part extruded at 670 °C, a consistent blocky structure was observed across the entire cross-section, from the center to the edge, suggesting an overall increase in temperature of over 100 °C from the center to the edge. The size of the α phase at the lower part of 670°C measures 12.5 ± 3.2 μm at the center and 11.3 ± 3.3 μm at the edge, respectively. This indicates that while there was a slight reduction in size towards the edge, the disparity was relatively minor in comparison to the upper and middle parts. Meanwhile, in the case of the upper part extruded at 730 °C, alpha phases displaying closer proximity to the Widmanstätten structure with anisotropic characteristics were observed at the center, whereas a blocky structure was observed at the edge. This discrepancy arises due to the higher heat generation resulting from frictional heat and plastic deformation at the edge, leading to a significant temperature increase. In contrast, the temperature rise at the center was not that high, indicating that the hot extrusion process was conducted within the (α + β) region. As for the middle and lower parts extruded at 730 °C, uniformly isotropic blocky structure was formed throughout the cross-section with α phase sizes of 22.6 ± 4.5 μm and 21.3 ± 4.6 μm for the center and edge of the middle part, and 18.6 ± 4.5 μm and 14.2 ± 4.2 μm for the center and edge of the lower part, respectively. A noteworthy observation is that, in the case of the blocky structure formation, there is a slight reduction in size towards

the edge compared to the substantial decrease observed in specimens exhibiting a Widmanstätten structure. In other words, the assessment of the cross-section revealed the existence of a uniform microstructure when a blocky structure was formed. This leads to the conclusion that when a blocky structure is formed, a more uniform microstructure is obtained even in a perpendicular direction to the extrusion direction.

4.3.2 Mechanical analysis

Furthermore, we conducted an evaluation of uniformity in the direction perpendicular to the extrusion axis, that is, radial direction of the specimen, using continuous hardness line scanning from the center to the edge. Fig. 4.9(a) and (b) indicate the Vickers hardness values depending on the distance from the center, measured from the upper, middle, and lower parts of the hot-extruded specimen at 670 ℃ and 730 ℃, respectively. In the upper and middle parts extruded at 670 ℃, as well as the upper part extruded at 730 ℃, all of which exhibit a Widmanstätten structure, there is notable scattering and large standard deviation values observed along the center to edge direction. Moreover, an increase in hardness was observed towards the edge, which can be attributed to the reduction in the size of the α phase. Conversely, in the case of the lower part extruded at 670 ℃, and the middle and lower parts extruded at 730 ℃, characterized by a blocky structure, uniform hardness values were observed across the cross-section due to the minimal deviation in the size of the α phase from the center to the edge. Moreover, the standard deviation at individual points exhibited relatively low values. Fig. 4.10 illustrates the average Vickers hardness values and corresponding standard deviations measured from twenty indentation tests conducted on each of the extruded specimens. Under the same extrusion temperature conditions, a consistent trend of increasing hardness values from the upper part to the lower part was observed, with the microstructural analysis showing an augmentation in the β' phase fraction and a reduction in the α phase size, as illustrated in Figs. 4.3 (a) and (b), respectively. Moreover, when comparing the same position, it was noticed that the upper parts with similar α

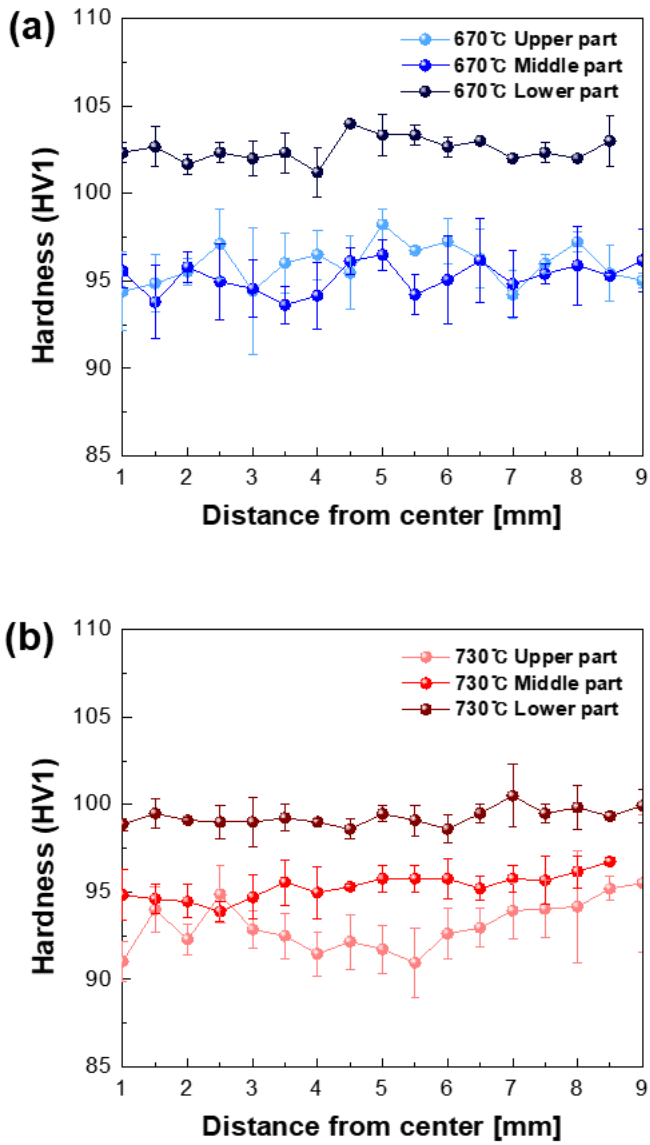

Figure 4.9 Vickers hardness values (HV1) depending on distance from the center obtained from upper, middle, and lower part of hot-extruded $Cu_{58}Zn_{39}Pb_3$ wt.% alloy at (a) 670 °C and (b) 730 °C

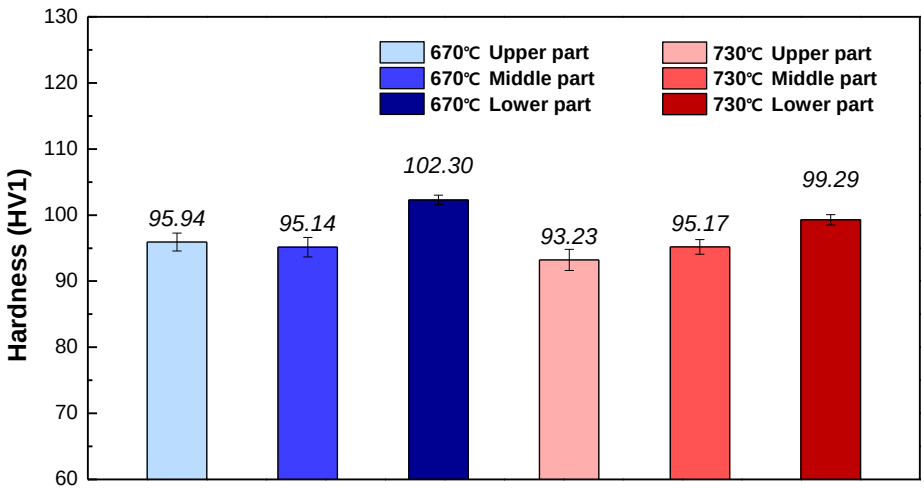

Figure 4.10 Vickers hardness values (HV1) obtained from upper, middle, and lower parts of hot-extruded $Cu_{58}Zn_{39}Pb_3$ wt.% alloy at 670 ℃ and 730 ℃

phase sizes exhibited approximately 3% higher hardness values in the 670 °C extruded sample, attributable to its higher β' phase fraction. In the middle part, despite a higher β' fraction in the 670 °C extruded sample, the larger α phase size resulted in same hardness values for both extrusion temperature conditions. Lastly, in the lower part, the 670 °C extruded sample indicates the highest hardness value due to both a smaller α phase size and higher β' phase fraction. In summary, the evaluation of the cross-section from the center to the edge leads to the following conclusions: (i) the formation of a uniform blocky structure is accompanied by uniform microstructure and hardness characteristics throughout the cross-section from center to the edge (ii) the fraction of the β' phase and the size of the α phase are the most critical factors to determine hardness.

4.4. Machinability evaluation of hot extruded $Cu_{58}Zn_{39}Pb_3$ wt.%

Drilling tests were conducted on the 670 ℃ extruded upper part and the 730 ℃ extruded lower part, which are anticipated to exhibit relatively limited and excellent machinability, respectively, based on their microstructure and mechanical properties. Additionally, a drilling test was performed on the lead-free brass alloy as a control group. A schematic description of the experimental setup and drilling operation used in this study for machinability evaluation was shown in Fig. 2.9. The change in rotation torque with the number of runs during the drilling test for each sample is shown in Fig. 4.11(a). As the drill made initial contact with the workpiece, the cutting area rapidly increased, and subsequently, the rotation torque is stabilized, establishing a fixed cutting area. In this stable region, the average rotation torque value is defined as a rotation torque for each sample. To ensure experimental accuracy, each specimen underwent three or more experiments, and the average value along with the standard deviation was represented in Fig. 4.11(b). The results in Fig. 4.11(a) and (b) indicate that the lead-free brass alloy exhibited approximately 30% higher rotation torque value compared to the other two specimens, indicating inferior machinability. On the other hand, the upper part extruded at 670 ℃ and the lower part extruded at 730 ℃ showed similar rotation torque values. The 670 ℃ extruded upper part exhibited approximately 2% higher rotation torque than the 730 ℃ extruded lower part. Through the evaluation of rotation torque for each specimen, it was established that the hot-extruded $Cu_{58}Zn_{39}Pb_3$ wt.% alloy demonstrates superior machinability compared to the lead-free brass alloy. However, due to the difficulties

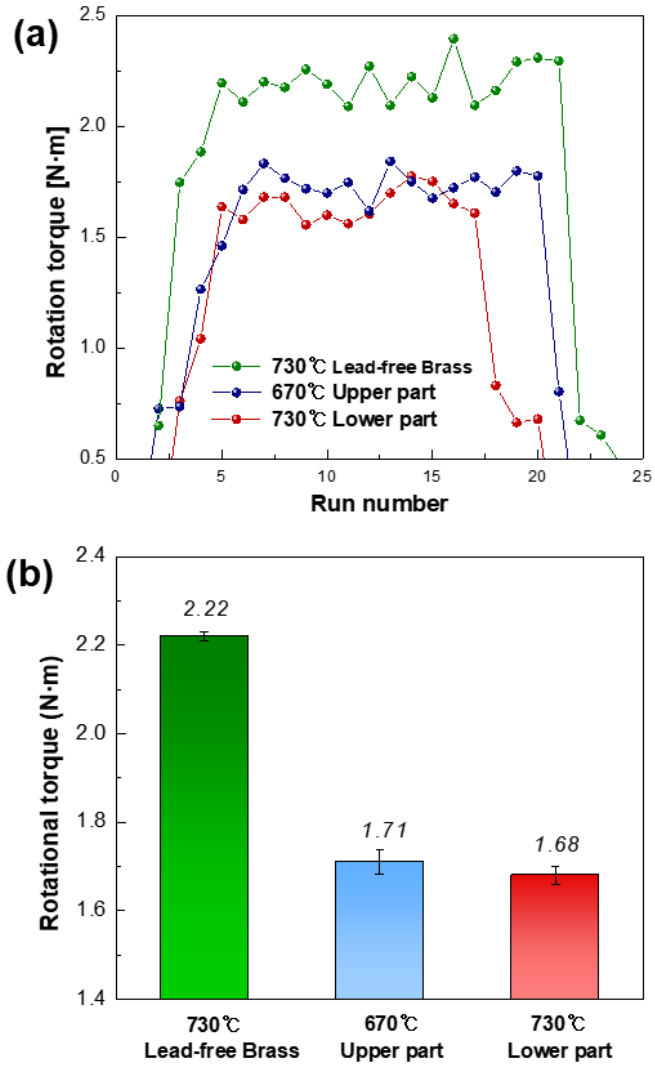

Figure 4.11 (a) Rotation torque depending on the run number during drilling process of hot-extruded $Cu_{58}Zn_{39}Pb_3$ wt.% alloy at 670 °C (blue) and 730 °C (red) (b) average rotation torque obtained from hot-extruded $Cu_{60}Zn_{40}$ wt.% alloy at 730 °C (yellow-green), $Cu_{58}Zn_{39}Pb_3$ wt.% alloy at 670 °C (sky blue) and 730 °C (red)

in directly comparing machinability based solely on quantitative rotation torque values for different extrusion temperature conditions for Cu58Zn39Pb3 wt.% alloy, we conducted a comprehensive assessment that included analyzing chip morphology and comparing the weight fraction of chips for each type.

Fig. 4.12(a) presents the chip morphologies obtained during the drilling test, categorized into A to E types based on their distinct cmophology as outlined in Table 4.2. Specifically, A and B types represent continuous chips in the form of long and short washer-type helical chips, respectively, while C, D, and E types correspond to discontinuous chips, characterized as loose arcs with one curl, loose arcs with half a curl, and elemental chips, respectively. Fig. 4.12(b) shows the weight fraction of chips for each type, indicated based on the classification of chips shown in (a1)-(a3), and detailed quantitative weight fractions are presented in Table 4.2. For the lead-free brass alloy, approximately 25.2% of the chips categorized under the continuous chip and D type was predominantly formed among the discontinuous chips at approximately 62.6%. In contrast, the 670 ℃ extruded upper part shows an absence of A type continuous chips, with only 4.1% accounting for B type, and D type remains dominant among the discontinuous chips at approximately 63.8%. Finally, the 730 ℃ extruded lower part, which was anticipated to exhibit superior machinability, completely lacks A type continuous chips, with formation of B type comprising only 0.5%. Especially, among the discontinuous chips, E type is significantly prominent at approximately 72.8%, indicating excellent machinability. Moreover, Fig. 12(c) provides the average weight per chip type for each specimen.

The results also reveal that the lead-free brass alloy demonstrates relatively high average weights for all chip types, indicating poor machinability. Conversely, the

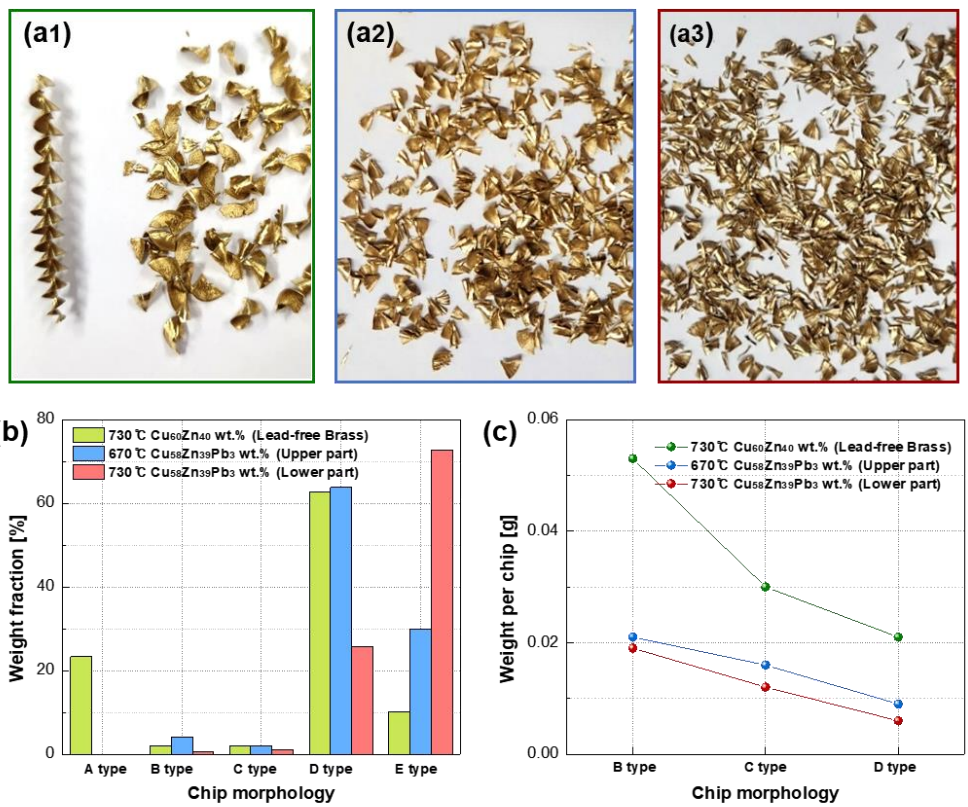

Figure 4.12 Morphology of Segmented chips after drilling process of (a1) hot-extruded $Cu_{60}Zn_{40}$ wt.% alloy at, (a2) hot-extruded $Cu_{58}Zn_{39}Pb_3$ wt.% alloy at 670 °C and (a3) 730 °C. (b) weight fraction and (c) weight per chip for each chip type obtained from hot-extruded $Cu_{60}Zn_{40}$ wt.% alloy at 730 °C (yellow-green), $Cu_{58}Zn_{39}Pb_3$ wt.% alloy at 670 °C (sky blue) and 730 °C (red)

	Chip Type	A Type	B Type	C Type	D Type	E Type
	Chip morphology					
		Continuous (Long washer type helical)	**Continuous** (Short washer type helical)	**Discontinuous** (Loose Arc - One curl)	**Discontinuous** (Loose Arc - Half a Curl)	**Discontinuous** (Elemental)
	Type of Curl Length l	> 5 Curl ($l \leq 50$mm)	1~5 Curl ($l \leq 50$mm)	≒ 1 Curl	< 1 Curl	The rest of the small crumbs
730℃ Lead-free ($Cu_{60}Zn_{40}$)	Weight fraction [%]	*23.3*	*2.0*	*2.0*	*62.6*	*10.1*
	Weight per chip [g]	*0.3439*	*0.053*	*0.030*	*0.021*	
670℃ extruded Upper part	Weight fraction [%]	*0*	*4.1*	*2.1*	*63.8*	*30.0*
	Weight per chip [g]		*0.021*	*0.016*	*0.009*	
730℃ extruded Lower part	Weight fraction [%]	*0*	*0.5*	*1.0*	*25.7*	*72.8*
	Weight per chip [g]		*0.019*	*0.012*	*0.006*	

Table 4.2 Classification of chips based morphology and weight fraction and weight per chip for each chip type obtained from hot-extruded $Cu_{60}Zn_{40}$ wt.% alloy at 730 ℃, $Cu_{58}Zn_{39}Pb_3$ wt.% alloy at 670 ℃ and 730 ℃

730 ℃ extruded lower part exhibits the lowest average weight, further verifying its excellent machinability. In particular, the reason why the machinability of the lead-free brass alloy is limited is that there is no lead acting as a lubricant, the fraction of the β' phase is the lowest at 31.8%, and the size of the α phase is the largest. Conversely, although the 670 ℃ extruded upper part exhibits a higher β' phase fraction compared to the 730 ℃ extruded lower part, the inferior machinability can be attributed to the presence of a relatively non-uniform distribution of Pb particles and the occurrence of a Widmanstätten structure. These irregularities and anisotropic structures are prone to induce stress concentration and shear localization during machining, resulting in the formation of voids and cracks. These phenomena are regarded as the primary factors contributing to the relatively low machinability. [35-37] Based on the comprehensive evaluation of machinability through drilling tests, it is evident that the lead-free brass alloy exhibits poor machinability, which limits its practical industrial use. On the other hand, interestingly, the upper part extruded at 670 °C still shows the predominant formation of discontinuous chips, suggesting potential industrial applicability, although the machinability is expected to be inferior according to the criteria of β phase fraction, α phase morphology and uniform distribution of Pb particles. This indicates that with machining optimization, including selection of tool, lubrication, and machining conditions, both the 670 ℃ and 730 ℃ extruded specimens can be successfully used for product manufacturing. Nevertheless, drawing conclusions from the chip analysis, as presented in Fig. 4.12(b) and (c), indicates that an extrusion temperature of 730℃ is more favorable. This choice facilitates the minimization of tool heat, tool wear, and additionally, it offers improved mechanical properties. Additionally, it is suggested

to consider increasing the extrusion temperature by about 10 – 20 ℃ and eliminating the residue of Widmanstätten structure at the center of the upper part extruded at 730 ℃. Nevertheless, certain potential factors must be carefully considered, such as the increase in production costs, the occurrence of hot shortness cracking, and the formation of surface oxidation.

4.5. Summary

In Section 4, a comprehensive investigation was conducted on the structural heterogeneity arising from the extrusion conditions of the duplex brass alloy. Initially, $Cu_{58}Zn_{39}Pb_3$ wt.% alloy samples were prepared by dividing the extrusion temperature into 670°C and 730°C as the first variable. Subsequently, the samples were further categorized based on their longitudinal and radial positions with respect to the extrusion direction for analysis.

In the analysis of the microstructure along the longitudinal direction, it was observed that depending on the extrusion temperature range, the specimens exhibited either a Widmanstatten structure in the $\alpha+\beta$ region or a blocky structure in the single β region. The different microstructures within the same extrusion temperature range can be attributed to the temperature variation, resulting from factors such as frictional heat between the brass alloy and the mold and heat generated during plastic deformation, inherent to the direct extrusion process. As the temperature increases from the upper to the lower part, the size of α phase decreases due to more severe plastic deformation and the subsequent increase in nucleation sites for recrystallization. The most significant difference in microstructure was observed between the 670°C upper part and the 730°C lower part specimens. The mechanical properties analyzed through tensile tests could be well correlated with the extended Hall-Petch relation, showing that the 730°C lower part specimen with smaller grain size had a higher yield strength.

Regarding the analysis of microstructure in the radial direction of the specimens, it was observed that the size of α phase decreased toward the edge. Direct extrusion

led to increased frictional heat and severe plastic deformation from the center to the edge of the cross-section, resulting in higher cooling rates at the edges. Consequently, the α phase exhibited relatively smaller sizes at the edges, leading to an increase in hardness along the radial direction. In contrast, when a blocky structure was formed, a more uniform microstructure was observed even in the direction perpendicular to the extrusion axis, and the hardness values were more uniform across the entire cross-section.

The evaluation of machinability through drilling tests revealed that the lead-free brass exhibited poor machinability due to the absence of lead, lower β' phase fraction, and larger α phase size. On the other hand, both the 670°C extruded upper part and the 730°C extruded lower part demonstrated dominant formation of discontinuous chips, indicating potential industrial applicability. Although the 730°C extruded lower part exhibited the best machinability, further consideration of potential factors such as increased production costs, hot shortness cracking, and surface oxidation is essential before making a final decision on the extrusion temperature optimization.

CHAPTER 5

Conclusion

In this investigation, we explored the impact of hot extrusion temperature on the microstructure, mechanical properties, and machinability of duplex brass alloy to propose optimal extrusion temperature conditions suitable for industrial-scale applications. To comprehend the influence of hot extrusion at different temperatures on the microstructure, we initially examined the as-cast alloy's microstructure with a specific focus on the distribution of Pb particles. Subsequently, we conducted extrusion at 670 ℃ (0.82 Tm) and 730 ℃ (0.87 Tm) to produce specimens of sizes used in industrial applications, and then systematically compared the microstructure in both the extrusion direction and the cross-section perpendicular to the extrusion direction. Finally, we carefully analyzed the mechanical properties and machinability of two specimens which have Widmanstätten and isotropic blocky structures.

The key insights from our study are as follows: (i) The as-cast duplex brass alloy with the Widmanstätten structure exhibited a heterogeneous distribution of Pb particles due to constitutional supercooling during solidification and the monotectic reaction from residual liquid to Pb particles and β phase. (ii) Comparing the upper, middle, and lower parts of the extruded specimens, we observed a gradual temperature increase from the upper to lower part, with a temperature difference exceeding 100 ℃. The upper and middle parts extruded at 670 ℃ underwent hot

extrusion in the (α + β) region, leading to the formation of Widmanstätten structured α phase with non-uniformly distributed Pb particles. Conversely, the middle and lower parts extruded at 730 °C were extruded within the single β phase region, leading to the formation of an isotropic blocky α phase characterized by uniformly distributed Pb particles. (iii) The 670 °C extruded lower part and the 730 °C extruded middle and lower parts displayed a uniform isotropic blocky α phase and consistent hardness values across the cross-section perpendicular to the extrusion direction. (iv) In comparing the 670 °C extruded upper part with Widmanstätten structure and the 730 °C extruded lower part with blocky structure, the latter demonstrated 22.8% higher yield strength and 21.2% lower ductility. Additionally, although both specimens exhibited the formation of discontinuous chips and the rotation torque was only 2% lower for the 730 °C extruded lower part, the 670 °C extruded upper part showed 63.8% of the loose arc of half a curl chips, while the 730 °C extruded lower part formed 72.8% elemental chips, indicating superior machinability for the latter.

Based on the investigation, it is recommended to choose a hot extrusion temperature of 730 °C within the (α + β) region to prevent the formation of anisotropic Widmanstätten structure and mitigate issues related to high extrusion temperature, such as cost wastage and hot shortness. Moreover, our findings offer valuable insights for optimizing the extrusion temperature of the duplex brass alloy by establishing a systematic correlation between hot extrusion temperature, microstructure in the extrusion and perpendicular directions, mechanical properties, and machinability.

Bibliography

[1] R. Haubner, S. Strobl, P. Linhardt, Effects on microstructure and corrosion behavior of a heat treated CuZn36Pb2 brass, Defect and Diffusion Forum, Trans Tech Publ, 2020, pp. 333-338.
[2] A.I. Toulfatzis, G.A. Pantazopoulos, C.N. David, D.S. Sagris, A.S. Paipetis, Machinability of eco-friendly lead-free brass alloys: Cutting-force and surface-roughness optimization, Metals 8(4) (2018) 250.
[3] A.A. Fadhil, M.S. Ghattas, B.A. Iskander, S.A. Ajeel, T.A. Enab, Structural characterization and detecting processes of defects in leaded brass alloy used for gas valves production, Alexandria engineering journal 57(3) (2018) 1301-1311.
[4] K. Aytekin, Characterization of machinability in lead-free brass alloys, 2018, p. 65.
[5] C.-C. Hsieh, J.-S. Wang, P.T.-Y. Wu, W. Wu, Microstructural development of brass alloys with various Bi and Pb additions, Metals and Materials International 19 (2013) 1173-1179.
[6] M. Akbari, P. Asadi, Optimization of microstructural and mechanical properties of brass wire produced by friction stir extrusion using Taguchi method, Proceedings of the Institution of Mechanical Engineers, Part L: Journal of Materials: Design and Applications 235(12) (2021) 2709-2719.
[7] M. Moriarty, Y. Wu, T. Murray, C. Hutchinson, The effect of phase fraction, size and shape on the dezincification of duplex brasses, Corrosion Science 184 (2021) 109366.
[8] J. Johansson, P. Alm, R. M'Saoubi, P. Malmberg, J.-E. Ståhl, V. Bushlya, On the function of lead (Pb) in machining brass alloys, The International Journal of Advanced Manufacturing Technology 120(11-12) (2022) 7263-7275.
[9] F. Schultheiss, D. Johansson, M. Linde, P.L. Tam, V. Bushlya, J. Zhou, L. Nyborg, J.-E. Ståhl, Machinability of CuZn21Si3P brass, Materials Science and Technology 32(17) (2016) 1744-1750.
[10] P. García, S. Rivera, M. Palacios, J. Belzunce, Comparative study of the parameters influencing the machinability of leaded brasses, Engineering Failure Analysis 17(4) (2010) 771-776.
[11] K.J. Al-Fadhalah, M. Aleem Rafeeq, N. Thomas, Microstructure and texture development in thermomechanically processed leaded brass, Metals 11(7) (2021) 998.
[12] Y. Ziat, M. Hammi, C. Laghlimi, A. Moutcine, Investment casting of leaded brass: Microstructure micro-hardness and corrosion protection by epoxy coating, Materialia 12 (2020) 100794.
[13] S.Z. Han, E.-A. Choi, S.H. Lim, S. Kim, J. Lee, Alloy design strategies to increase strength and its trade-offs together, Progress in Materials Science 117 (2021) 100720.

[14] G. Pantazopoulos, A. Vazdirvanidis, Characterization of the microstructural aspects of machinable-phase brass, Microscopy and analysis 22(5) (2008) 13-16.
[15] A.I. Toulfatzis, G.J. Besseris, G.A. Pantazopoulos, C. Stergiou, Characterization and comparative machinability investigation of extruded and drawn copper alloys using non-parametric multi-response optimization and orthogonal arrays, The International Journal of Advanced Manufacturing Technology 57(5) (2011) 811-826.
[16] F. Schultheiss, D. Johansson, V. Bushlya, J. Zhou, K. Nilsson, J.-E. Ståhl, Comparative study on the machinability of lead-free brass, Journal of Cleaner Production 149 (2017) 366-377.
[17] C. Nobel, F. Klocke, D. Lung, S. Wolf, Machinability Enhancement of Lead-free Brass Alloys, Procedia CIRP 14 (2014) 95-100.
[18] N. Zoghipour, E. Tascioglu, Y. Kaynak, Machinability of extruded and multi-directionally hot forged eco-friendly brass alloys, Canadian Metallurgical Quarterly (2023) 1-12.
[19] A. Wolfenden, P. Wright, Role of lead in free-machining brass, Metals Technology 6(1) (1979) 297-302.
[20] N. Ånmark, A. Karasev, P.G. Jönsson, The effect of different non-metallic inclusions on the machinability of steels, Materials 8(2) (2015) 751-783.
[21] G. Pantazopoulos, Leaded brass rods C 38500 for automatic machining operations: A technical report, Journal of Materials Engineering and Performance 11(4) (2002) 402-407.
[22] C. Mapelli, R. Venturini, Dependence of the mechanical properties of an α/β brass on the microstructural features induced by hot extrusion, Scripta materialia 54(6) (2006) 1169-1173.
[23] A. Bhaduri, Mechanical properties and working of metals and alloys, Springer2018.
[24] K. Holler, B. Reetz, K.B. Müller, A. Pyzalla, W. Reimers, Microstructure and Properties of Hot Extruded Brass CuZn40Pb2, Materials Science Forum 426-432 (2003) 3667-3672.
[25] A.F. Castle, Extrusion, ASM International2006.
[26] R. Vargas, V. Gonda, L. Ruiz, Thermal analysis and control for heating of an extrusion die, Bánki Közlemények (Bánki Reports) 1(1) (2018) 63-66.
[27] R. Goswami, K. Chattopadhyay, P. Ryder, Melting of Pb particles embedded in Cu–Zn matrices, Acta Materialia 46(12) (1998) 4257-4271.
[28] A. OHNO, Formation mechanism of the equiaxed chill zone in ingots, Transactions of the Iron and Steel Institute of Japan 10(6) (1970) 459-463.
[29] M. Sadayappan, J. Thomson, M. Elboujdaini, G.P. Gu, M. Sahoo, Grain refinement of permanent mold cast copper base alloys, Copper Development Association (US), 2005.
[30] G. Tkachuk, O. Chikova, V. Maltsev, Examining microstructure of

industrial brass blanks with purpose for quality control in respect of defects of technological origin, IOP Conference Series: Earth and Environmental Science, IOP Publishing, 2017, p. 092027.
[31] Y.N. Loginov, A.S. Ovchinnikov, Increase in the Uniformity of Structure and Properties of Extruded Workpieces of Alpha + Beta Lead Brasses, Metallurgist 59(3-4) (2015) 342-347.
[32] S.E. Mousavi, M. Meratian, A. Rezaeian, Investigation of mechanical properties and fracture surfaces of dual-phase 60–40 brass alloy processed by warm equal-channel angular pressing, Journal of Materials Science 52 (2017) 8041-8051.
[33] G. Pashos, G.A. Pantazopoulos, I. Contopoulos, A comprehensive CFD model for dual-phase brass indirect extrusion based on constitutive laws: Assessment of hot-zone formation and failure prognosis, Metals 8(12) (2018) 1043.
[34] S. Rahim, M. Lajis, S. Ariffin, Effect of extrusion speed and temperature on hot extrusion process of 6061 aluminum alloy chip, ARPN J. Eng. Appl. Sci 11(4) (2016) 2272-2277.
[35] M. Adineh, H. Doostmohammadi, R. Raiszadeh, Effect of Si and Al on the microstructure, mechanical properties and machinability of 65Cu-35Zn brass, Iran. J. Mater. Sci. Eng 16(2) (2019).
[36] U. Hofmann, E. El-Magd, Behaviour of Cu-Zn alloys in high speed shear tests and in chip formation processes, Materials Science and Engineering: A 395(1-2) (2005) 129-140.
[37] Ö. Semih, A. Recep, Investigation of microstructure, machinability, and mechanical properties of new-generation hybrid lead-free brass alloys, High Temperature Materials and Processes 42(1) (2023) 20220263.
[38] P. Stavroulakis, A.I. Toulfatzis, G.A. Pantazopoulos, A.S. Paipetis, Machinable leaded and eco-friendly brass alloys for high performance manufacturing processes: A critical review, Metals 12(2) (2022) 246.
[39] Y. Chou, Dislocation pileups and the Hall–Petch relation, Canadian Journal of Physics 45(2) (1967) 559-566.
[40] E. Werner, H.P. Stüwe, Phase boundaries as obstacle to dislocations motion, Materials Science and Engineering 68(2) (1985) 175-182.
[41] P. Lehto, H. Remes, T. Saukkonen, H. Hänninen, J. Romanoff, Influence of grain size distribution on the Hall–Petch relationship of welded structural steel, Materials Science and Engineering: A 592 (2014) 28-39.
[42] B. Roebuck, Measurement of grain size and size distribution in engineering materials, Materials science and technology 16(10) (2000) 1167-1174.
[43] C. Stoddart, C. Lea, W. Dench, P. Green, H. Pettit, Relationship between lead content of Cu–40Zn, machinability, and svvarf surface composition determined by Auger electron spectroscopy, Metals Technology 6(1) (1979) 176-184.

[44] N. Zoghipour, E. Tascioglu, G. Atay, Y. Kaynak, Machining-induced surface integrity of holes drilled in lead-free brass alloy, Procedia CIRP 87 (2020) 148-152.
[45] G. Pantazopoulos, A. Vazdirvanidis, Failure analysis of a fractured leaded-brass (CuZn39Pb3) extruded hexagonal rod, Journal of Failure Analysis and Prevention 8(3) (2008) 218-222.
[46] N. Gane, The effect of lead on the friction and machining of brass, Philosophical Magazine A 43(3) (1981) 545-566.
[47] Z. Fan, P. Tsakiropoulos, P. Smith, A. Miodownik, Extension of the Hall-Petch relation to two-ductile-phase alloys, Philosophical Magazine A 67(2) (1993) 515-531.
[48] Z. Fan, Microstructure and mechanical properties of multiphase materials, University of Surrey (United Kingdom)1993.
[49] J. Johansson, H. Persson, J.-E. Ståhl, J.-M. Zhou, V. Bushlya, F. Schultheiss, Machinability evaluation of low-lead brass alloys, Procedia Manufacturing 38 (2019) 1723-1730.

Abstract in Korean

초 록

열간 압출 유연 황동 합금의 구조적 특성에 관한 연구

이지은

서울대학교 공과대학

재료공학부

황동합금(Cu-Zn계 합금)은 연성, 가공성이 우수함과 동시에 내산화성이 우수하여 복잡한 형상가공이 필요한 수전 관련 부품에 널리 사용되는 소재이다. 그 중 납이 포함된 유연황동합금(Cu-Zn-Pb 합금)의 경우 절삭시 납이 압출 공정은 금형의 모양과 크기에 따라 다양한 제품을 만들 수 있는 장점이 있으나 열간 압출이 진행됨에 따라 마찰에 의해 온도가 상승하여 여러 가지 문제점을 야기한다. 특히 열간 직접 압출의 경우 마찰열과 소성가공시 발생하는 여분의 열로 인하여 따라서 압출시 공정 결함을 최소화하면서도 공정에 필요한 에너지를 절약 가능한 이점을 가질 수 있는 압출 온도 범위의 최적화가 필요하다.

본 논문은 열간압출공정 상에서 유연황동합금의 구조적 특성에 관한 연구로, 미세구조 및 기계적특성을 분석하여 이와 절삭성과의 상관관계를 이해하고자 하였다. 부연하며, 절삭성이 우수한 합금인 $Cu_{58}Zn_{39}Pb_3$ 조성

의 상용제품에 대하여 산업적 대형 스케일에서의 공정 최적화를 위해 열간압출공정에 따른 미세구조 변화를 압출 온도 및 시편 위치에 따라 면밀하게 관찰하였다. 이때, Widmanstätten 구조가 나타났던 주조 시편이 압출이 이루어지는 온도 영역에 따라 미세구조상에서 homogeneity가 다르게 나타나는 것을 확인하였고, Vickers hardness test와 Uniaxial tensile test를 통해 기계적 특성 또한 미세구조의 homogeneity와 연관지어 해석하였다. 최종적으로는 드릴링 절삭성 평가를 진행함으로써, 미세구조 및 기계적 특성과 절삭성과의 관계를 알아보고자 하였다. 분석 결과를 통해 소성가공시 발생하는 열로 인하여 상태도 상에서의 beta 안정 평형 온도보다 낮은 온도에서 압출을 시행하여도 안정적으로 단일 beta 영역에서 압출이 가능함을 확인하였으며, 절삭성 개선을 위해서는 기계적 특성 뿐만 아니라 blocky 구조의 alpha 상을 가지면서 균일한 분포의 Pb가 중요한 역할을 하는 것을 확인할 수 있었다. 위 결과를 바탕으로 본 논문은 유연황동합금의 실제 상용제품에 대한 산업적 대형 스케일에서 온도 제어를 통해 공정 결함을 최소화하면서 에너지를 절약할 수 있는 열간압출공정의 최적화에 기여할 수 있을 것으로 기대된다.

핵심어 : 유연 황동, 열간 압출, 압출 온도, 기계적 특성, 절삭성

학번: 2021-24715